uc3m | Universidad Carlos III de Madrid

University Degree in Biomedical Engineering
2017-2018

Bachelor Thesis

"Advanced Image Reconstruction for Limited View Cone-Beam CT"

Xiaolin Ye

Director: Mónica Abella García

Co-Director: Nerea Ballesteros Tenrero

Leganés, 1 July 2018

[Include this code in case you want your Bachelor Thesis published in Open Access University Repository]
This work is licensed under Creative Commons **Attribution – Non Commercial – Non Derivatives**

ABSTRACT

In a standard CT acquisition, a high number of projections is obtained around the sample, generally covering an angular span of 360º. However, complexities may arise in some clinical scenarios such as surgery and emergency rooms or Intensive Care Units (ICUs) when the accessibility to the patient is limited due to the monitoring equipment attached. X-ray systems used in these cases are usually C-arms that only enable the acquisition of planar images within a limited angular range. Obtaining 3D images in these scenarios could be extremely interesting for diagnosis or image guided surgery. This would be based on the acquisition of a small number of projections within a limited angular span. Reconstruction of these limited-view data with conventional algorithms such as FDK result in streak artifacts and shape distortion deteriorating the image quality. In order to reduce these artifacts, advanced reconstruction methods can be used to compensate the lack of data by the incorporation of prior information.

This bachelor thesis is framed on one of the lines of research carried out by the Biomedical Imaging and Instrumentation group from the Bioengineering and Aerospace Department of Universidad Carlos III de Madrid working jointly with the Hospital General Universitario Gregorio Marañón through its Instituto de Investigación Sanitaria. This line of research is carried out in collaboration with the company SEDECAL, which enables the direct transfer to the industry.

Previous work showed that a new iterative reconstruction method proposed by the group, SCoLD, is able to restore the altered contour of the object, suppress greatly the streak artifacts and recover to some extend the image quality by restricting the space of search with a surface constraint. However, the evaluation was only carried out using a simulated mask that described the shape of the object obtained by thresholding a previous CT image of the sample, which is generally not available in real scenarios. The general objective of this thesis is the designing of a complete workflow to implement SCoLD in real scenarios.

For that purpose, the 3D scanner *Artec Eva* was chosen to acquire the surface information of the sample, which was then transformed to be usable as prior information for SCoLD method.

The evaluation done in a rodent study showed high similarity between the mask obtained from real data and the ideal mask obtained from a CT. Distortions in shape and streak artifacts in the limited-view FDK reconstruction were greatly reduced when using the real mask with the SCoLD reconstruction and the image quality was highly improved demonstrating the feasibility of the proposal.

Keywords: X-ray imaging, Limited-view Tomography, Advanced Reconstruction, 3D Scanner

ACKNOWLEDGEMENTS

For the accomplishment of a thesis like this, there is always an enormous amount of effort done additionally to the actual work.

To who brought me to the laboratory, Mónica, for showing me this awesome working place, helping me with any doubt and giving me such opportunities, this work would not have been possible without her.

To all colleagues of LIM that accompanied me in this journey, especially to Nerea, Claudia and Cristóbal, for their support, tireless help and kindness.

To *Chicuelas* for being with me all these years, listening and understanding me when frustrated, counting on me like always and made these four years unforgettable and special.

There is usually a way of calling these works as “End of Degree Thesis”, probably because it symbolizes the finish of an important stage in which we grow up in a most drastic and but less noticeable way.

I am grateful to study what I studied, to meet the people I met and had the chance to be next to them.

“我不去想

是否能够成功

既然选择了远方

便只顾风雨兼程

我不去想

身后会不会袭来寒风冷雨

既然目标是地平线

留给世界的只能是背影”

——汪国真 《热爱生命》

INDEX OF CONTENTS

INDEX OF FIGURES

INDEX OF TABLES

1 INTRODUCTION

1.1 INTRODUCTION TO X-RAYS

The discovery of the X-rays was made in 1895 by the German physicist W.C. Roentgen during an experiment with a cathode tube (Fig. 1.1 left). By applying a high voltage to it, an invisible light was appearing on a screen far away from the source, which was named as “X” referring to an unknown quantity. He also noticed that the X-rays can travel through solid materials casting shadows on a film.

Many scientists duplicated his experiment and gave to X-rays a variety of uses that were not clinically intended, such as shoe fitting or security control. Furthermore, within six months of the discovery, surgeons were able to use X-rays to locate bullets and examine the bone injuries since Roentgen also found out that human tissue and metallic objects appear to be different on the captured images (Fig. 1.1 right).

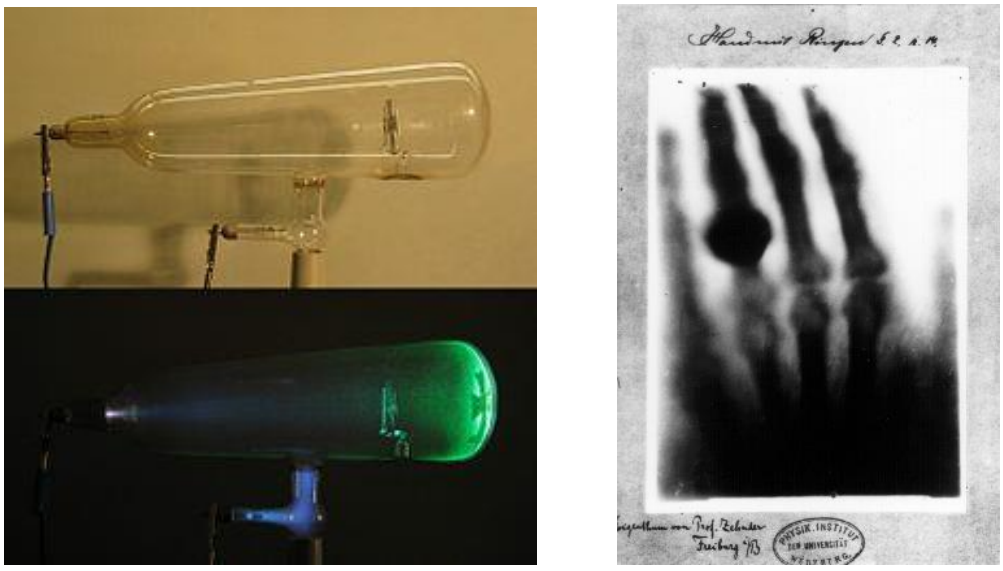

Fig. 1.1: Example of Crookes tubes used by Roentgen (left); the first hand X-ray image of Roentgen’s wife (right).

As soon as X-ray experiments were wildly performed, its hazardous nature was gradually observed. It was first reported at Vanderbilt University because of the hair loss of a scientist [1]. While more cases of X-ray burns were reported, many physicians claimed that it is harmless, until the death of *Elizabeth Fleischman* due to her involvement with X-rays, confirmed the risk of its usage.

Because of the huge interest of X-ray imaging, it has been continuously developed and diverged into several modalities. The most known modalities nowadays are Radiography (plain X-rays), Computed Tomography (CT), Mammography, Angiography and Fluoroscopy. The primary aim of all these modalities is the diagnosis and examination of the imaged area, which can be either bone, mammary tissue, blood vessel distribution or a certain organ.

In this section of the thesis, the basic physical principles of X-ray generation and detection will be explained for the acquisition of a useful image.

1.1.1 X-ray generation

According to Planck's description (Eq. 1.1) of high energetic Electromagnetic (EM) waves, X-rays can be described as a flux of photons in which each particle has an energy corresponding to the oscillation wavelength/frequency:

$$E = \frac{h \cdot c}{\lambda} = h \cdot v \qquad \text{(Eq. 1.1)}$$

where h stands for Planck's constant and has the value of $4.135 \cdot 10^{-15}\ eV \cdot s$, c is the speed of light, λ is the wavelength and v is the frequency.

The X-rays range from 100 eV to 100 KeV, which corresponds to wavelengths from 0.01nm to 10 nm or, equivalently in terms of frequency, from $3 \cdot 10^{16}\ Hz\ to\ 3 \cdot 10^{19}\ Hz$. This range is defined by grouping all the energies higher than UV rays and lower than gamma rays (Fig. 1.2). Within this interval, a further classification can be made according to their energy levels. Soft X-rays (from 10 nm to 0.1nm/100pm wavelength), due to their ease to be absorbed and their lower reflectivity than UV rays, are used for X-ray microscopy and produce images of very small structures. On the other hand, X-ray crystallization, radiographic images or security checks are done using hard X-rays. Therefore, when talking about medical imaging, it is taken as reference exclusively the range of 10KeV to 150 KeV [2].

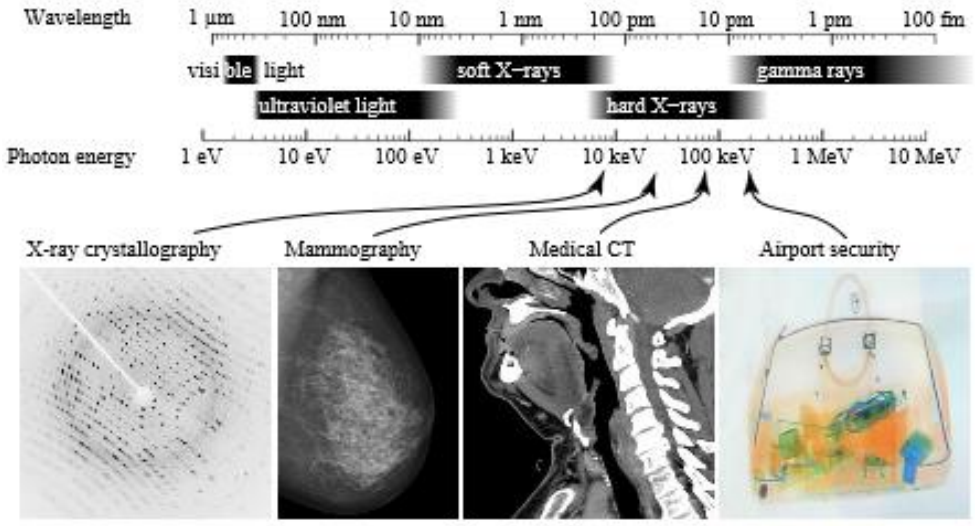

Fig. 1.2: Electromagnetic spectrum with examples of specific applications of hard X-rays.

The generation of the X-ray photons is commonly achieved in a vacuum tube (Fig. 1.3) covered with heavy materials leaving a window from where X-ray photons exit, a high voltage is applied across to both ends.

During X-ray generation, the filament heats up and emit electrons through thermionic emission. The accelerating flux of electrons travels from the cathode (tungsten filaments) and hit the surface of the target of the anode (tungsten except in mammography.). In this process, the kinetic energy that electrons gained is partially transformed into photons (4%), while the rest is all dissipated in the form of heat on the anode so that it has to be rotating to avoid overheating in a given portion of it.

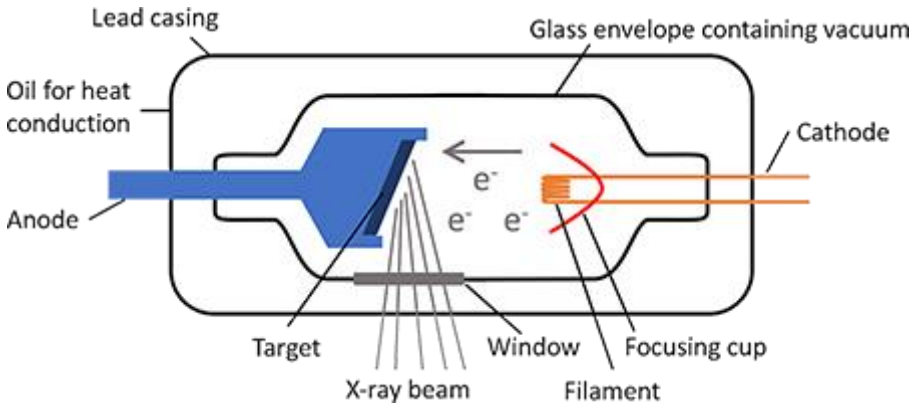

Fig. 1.3: Example scheme of an X-ray vacuum tube with essential components shown.

When accelerated electrons hit the target, two main processes may occur:

a) Bremsstrahlung or Braking Radiation

The interaction of incident electrons with the nucleus of the target atoms forces them to decelerate and give up part of their energy in the form of a photon. This interaction is due to the Coulomb's Force between particles of different charges and the resulting intensity of Bremsstrahlung radiation is governed by Kramer's Law (Eq. 1.2), where Z is the atomic number of the target material and e is the charge of the incident particle and m is its mass. This equation also explains the choice of electrons to be the collision particles (low mass) and the preference of high-Z target materials.

$$I_{Bremsstrahlung} \propto \frac{Z^2 z^4 e^6}{m^2} \qquad \text{(Eq. 1.2)}$$

The radiation spectrum given by this interaction is a continuous function where the probability of striking directly the nucleus and giving up all kinetic energy of the incident particle is minimal while the probability of giving up a portion of its kinetic energy as the form of photon is the highest (Fig. 1.4). These decelerated particles can also continue reacting with neighbor atoms and create more low energy photons.

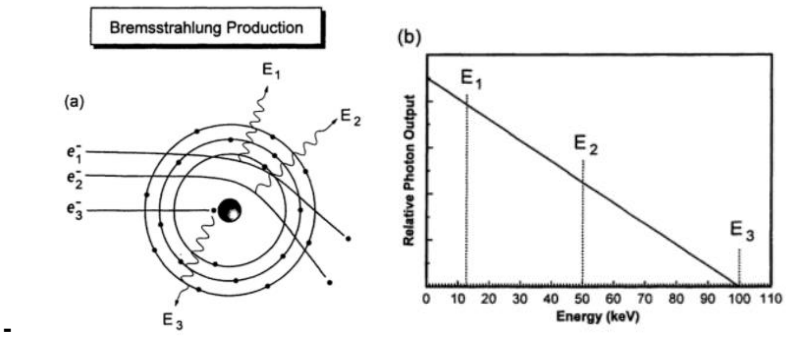

Fig. 1.4: Bremsstrahlung production scheme. (a) Electrons may either hit straight to the nucleus or be deviated at a certain distance to it. (b) The relative photon output depending on the incident energy of electrons. Source: [2]

b) Characteristic Radiation

The accelerated electrons can also interact with the electron cloud of the target material. Depending on the material used as target, a specific energy level distribution of its electrons can be found. The ejection of electrons from target atoms can occur when the kinetic energy gained by bombarding particles is higher than their binding energy. An electron in K shell (the innermost shell) of tungsten has a binding energy of 70keV while some other materials may have a lower binding energy. As in Bremsstrahlung production, successive interactions of both bombarding and ejected electron may take place until their kinetic energy reduces drastically.

As illustrated in Fig. 1.5 (left), the accelerated electron kicks out an orbital electron, and its position is covered by an outer shell electron. This movement releases energy, the so called Characteristic Radiation. The reduction in released intensity at low energies in a common X-ray spectrum (Fig. 1.5 right) is due to the ease of low energy photons to be absorbed by matter preventing them from travelling as far as others. Commonly, a previous filter is placed at the window of the X-ray tube in order to stop these particles before they reach the object

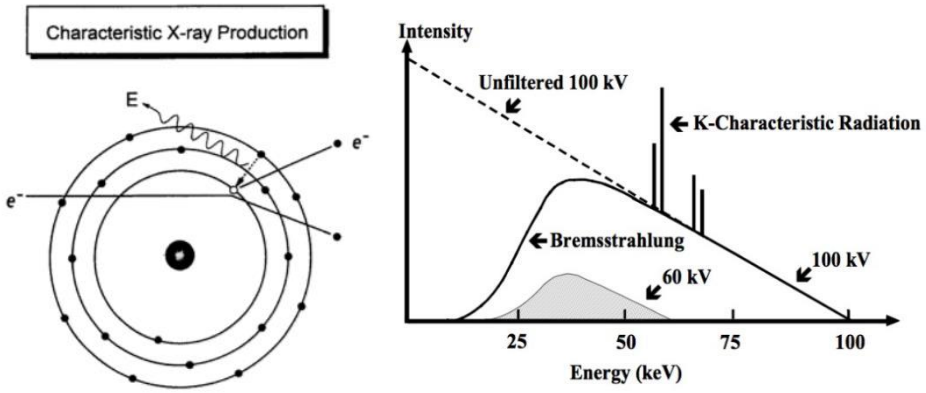

Fig. 1.5: Scheme of characteristic X-ray production is given (left). The release of energy are represented as sharp peaks on the basis of a Bremsstrahlung radiation spectrum (right) since the energies released are those corresponding to specific transitions. Source: [2]

The gap created by kicking out an electron is filled with electrons from next outer shell and so on, this successive process is known as the cascade of electronic transitions and

it ends with the filling of outermost shell gap with free electrons within the environment that lost their entire kinetic energy after reacting with neighbor atoms.

These transitions in energy levels result in the release of energies which are determined by their difference in binding energy. Since the description of energy levels is done by known discrete numbers, the emission energy corresponding to a specific transition for a given material can be calculated as stated in Eq. 1.3:

$$E_{characteristic} = E_{ini} - E_{end} \qquad \text{(Eq. 1.3)}$$

where the characteristic radiation energy, $E_{characteristic}$ will be the difference between the binding energy of the initial level, E_{ini}, and that of the ending level, E_{end}. Transitions between adjacent shells are called α transitions, and transitions between two or more shells are called β transitions. The most predominant transitions are the ones that land on the innermost K shell and these energy emissions contribute to the previous Bremsstrahlung spectrum as two sharp maxima (Fig. 1.5).

1.1.2 X-ray Interactions

Once the X-rays are produced, different interactions may occur between the incident photons and the atoms of the object to be imaged [2]:

a) Photoelectric effect

It is an ionization process in which incident photons give up their kinetic energy to one of the electrons of the target atom and ejecting it from its orbit. This process is only possible when the incident energy is higher or equal to the binding energy of the target electron. A vacancy will be created on the position where the ejected electron occupied and it can be located at the inner shell or outer ones depending on the amount of energy that the incident photon was carrying. Thus this vacancy may cause a cascade of electronic transitions and the eventual filling of the outermost shell with a free electron.

b) Rayleigh scattering

It describes the process in which the incident photon is reemitted with the same energy and an altered trajectory (thus also referred as elastic scattering). Therefore, contrary to the previous interaction, it is not ionizing and undesired for medical imaging since it makes difficult to know from which direction it comes originally and thus adds errors to the final image. In general, this process is more frequent in low energy photons at high-Z medium.

c) Compton scattering

It is considered as inelastic scattering since the deviated photon loses part of its energy by transferring it into an electron (most likely the outermost ones) causing ionization.

An illustration of phenomena described is shown in Fig 1.6:

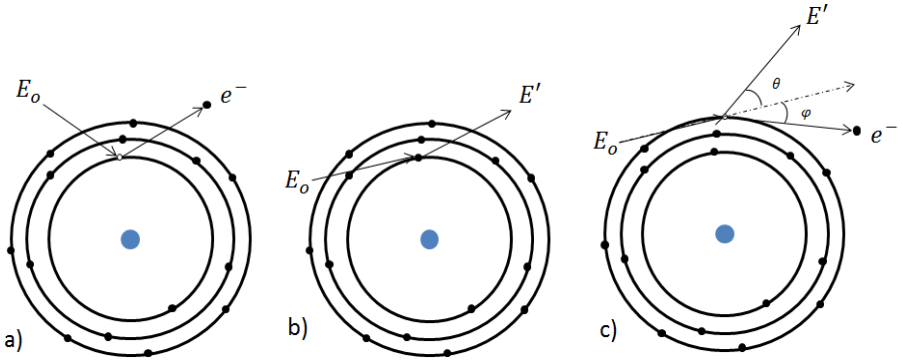

Fig. 1.6: Diagrams of X-ray interaction with matter being a) photoelectric effect, b) Rayleigh scattering and c) Compton scattering.

1.1.3 X-ray Detection

X-rays passing through the imaged object are collected using X-ray detectors for the image formation. One of the most common detectors were radiographic films (Fig. 1.7), which are made of silver halide emulsion and protected by gelatin. These films, when exposed to light, experience changes in the crystal structures of silver halide and make the area opaque and form a viewable image. Intensifying screens were added to increase the Signal to Noise Ratio (SNR) since the film was very sensitive to any light source. However, the inconvenience of manipulation, processing, dose reduction and storage encouraged the development of digital detectors.

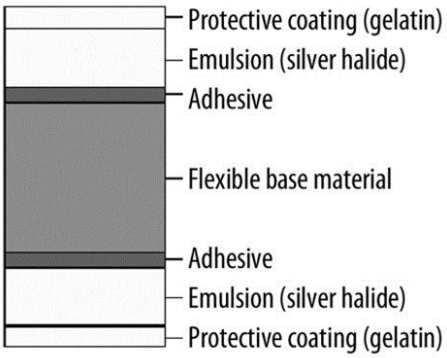

Fig. 1.7: Structure of a radiographic film where constituent layers can be observed. Source: [3]

Digital Radiography (DR) started to replace the primitive X-ray films from 1990s and its main advantage is the reduction on dose and the immediate image viewing capability. The most common ones are those called Flat Panel Detectors (FPD). Through an indirect procedure, the X-rays are first converted to light by a scintillator and then channeled through the amorphous silicon photodiode layer transforming the light received into a digital output signal.

With these devices, expensive film processing steps were eventually eliminated; a wider dynamic range can be achieved; imaging processing techniques are able to enhance the quality of the images and an easier access of the archives is possible.

1.2 PLANAR X-RAY IMAGING MODALITIES

X-rays can be used to reveal the internal structures of the body, resulting useful for clinical diagnosis. Since different tissues have different densities, each one will absorb or attenuate a given amount of incoming X-rays. Therefore, the X-ray image presents different contrasts depending on the density map of the tissues.

1.2.1 Projection

When recording the radiation emitted by the X-ray source after its attenuation by the object, the image formed presents the modulated distribution of radiation intensity and always offers a superposition image (Fig. 1.8). That is, all volume elements passed by any ray contribute to the attenuation of the radiation intensity [4]. In mathematical terms (Eq. 1.4), obtaining a projection image is equivalent to compute the attenuation provided by the object along the trajectory of the X-rays. This parameter is expressed as $\mu(\varepsilon)$ in Beer Lambert Law:

$$I = \int I_O(\varepsilon) \cdot e^{-\int \mu(\varepsilon) \cdot dx} d\varepsilon \qquad \text{(Eq. 1.4)}$$

where I is the photon intensity received by the detector, $I_O(\varepsilon)$ is the energy dependent intensity spectrum of the incident X-ray, $\mu(\varepsilon)$ is the attenuation coefficient of the material which represents the probability of the material to attenuate the photons and x describes the length of the material traversed.

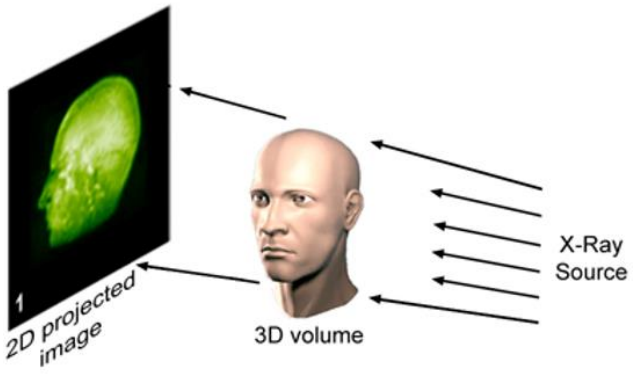

Fig. 1.8: Schematic of projection formation

1.2.2 Radiography

Conventional radiography uses regular radiographic films in which the images are not displayed directly after acquisition, but it requires complex procedures for the development, fixation, rinsing and drying of the films.

Digital radiography shares the same working principle as conventional radiography, except for the fact that the detectors are digital. This allows for less dangerous, faster and easily storable acquisitions. Once the projection is transferred from the detector to a computer screen they can be view immediately.

In this type of configuration (Fig. 1.9), the detector is a flat panel located at one side of the object while the source is at the other.

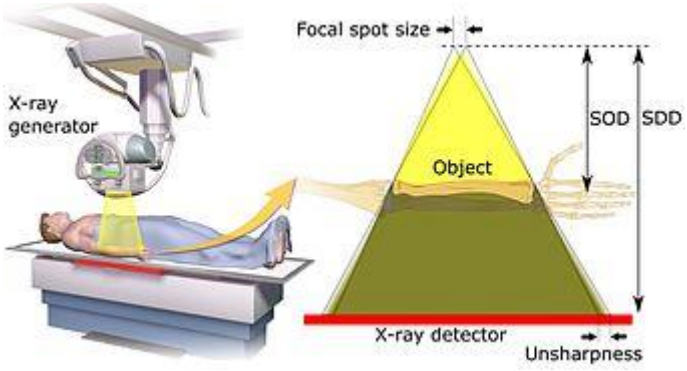

Fig. 1.9: A common acquisition scene is represented (left) and the origin of the magnification is represented with a scheme (right).

The magnification of the object on the final image can be easily derived from the Source-Object Distance (SOD) and Source-Detector Distance (SDD):

$$M = \frac{SDD}{SOD} \qquad \text{(Eq. 1.5)}$$

with $SDD = SOD + ODD$; and ODD stands for Object-Detector Distance.

An example of a projection obtained by conventional radiography can be seen in Fig. 1.10.

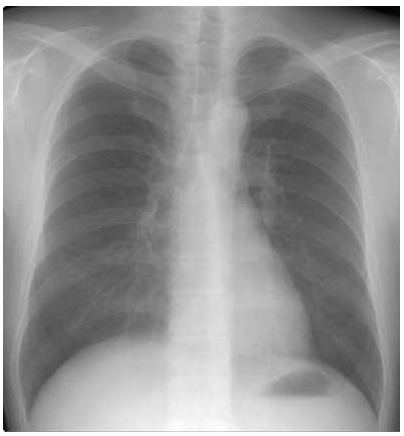

Fig. 1.10: Example of a chest radiography

1.2.3 Fluoroscopy

Fluoroscopy is an imaging technique that uses X-rays in a given time-span allowing the viewing of both anatomical and functional information. A fluorescence compound is

usually swallowed or injected on the region of interest to enhance the contrast within the soft tissue since they share similar values of density (Fig. 1.11). Also, by imaging the area several times, movements of organs such as heart or lungs can be detected. This technique is very helpful both for diagnosis and therapy and it is mostly used for image guided surgeries. Meanwhile, the radiation dose of this procedure is much higher than regular radiography due to the continuous acquisition.

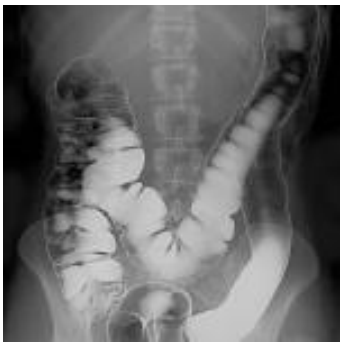

Fig. 1.11: Example result of fluoroscopy in abdomen.

1.2.4 C-arm

Contrary to stationary systems, C-arm is a mobile X-ray based device mostly used in operation rooms, where the accessibility to the patient is low and real time images are desired. The name of C-arm is given by is C shape element that connects on the one side the X-ray source and the detector or the image intensifier on the other side. Due to its flexibility and fluoroscopic capability, it is widely used for angiography and cardiac studies.

Conventional C-arm systems usually scope up to 150º orbital movement and are mainly used as planar imaging equipment (Fig. 1.12). With the high interest on 3D real-time visualization in surgery rooms, many efforts have been made regarding its architecture to enable tomographic capabilities. However, challenges associated with its mechanical instability and artifact prone nature are still present [5, 6].

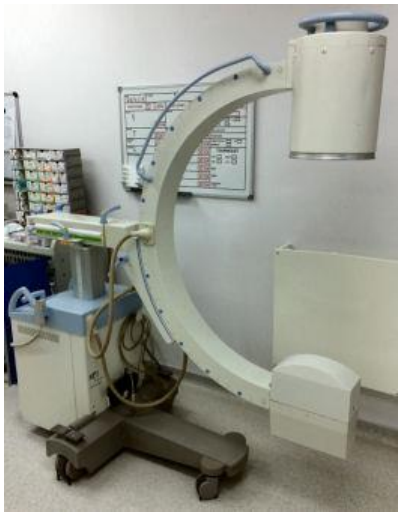

Fig. 1.12: A conventional C-arm system.

1.3 COMPUTED TOMOGRAPHY (CT)

CT was the first widely used radiological imaging modality which exclusively provided computed digital images instead of the well-known directly acquired analog images. It offers images of single discrete slices instead of superposition images of complete body sections [4].

The 3D image is achieved by taking several projections at different angles and using reconstruction algorithms to calculate the density values of the object (Fig. 1.13).

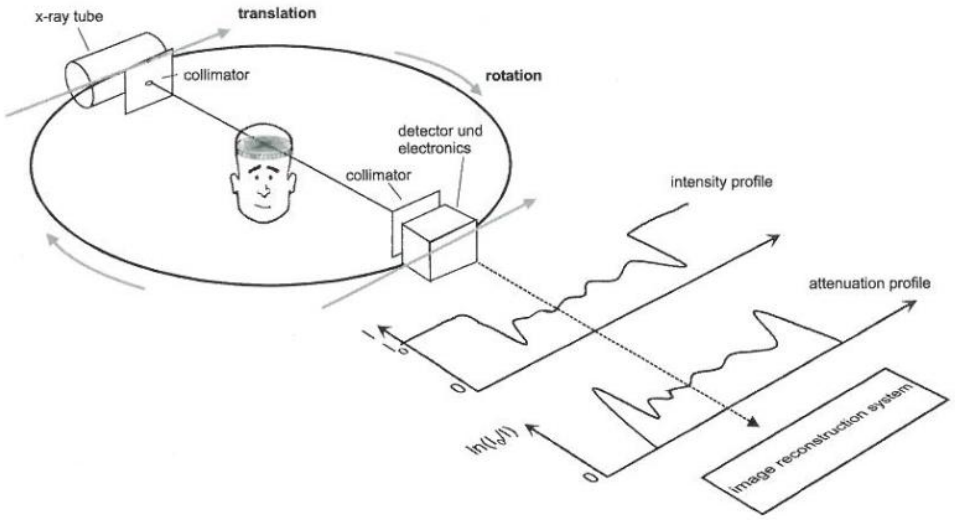

Fig. 1.13: Schematic of a CT image formation. The steps are (from left to right): X-ray emission, output X-ray detection as intensity profile, translation into attenuation profile and image reconstruction with several projections.

According to the complexity on geometry, CT systems can be ordered as follows:

a) Parallel Beam /Pencil Beam Geometry

The X-rays are emitted from a point source and the detector follows a rectilinear path (Fig. 1.14) parallel to the source until all the desired area is scanned. Moreover, the source has to be rotated for the acquisition of next projection in a different angle and repeat the process as many times as the number of projections needed.

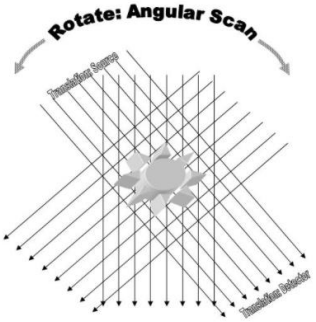

Fig. 1.14: Diagram of a parallel beam acquisition geometry. The lines represent the path of emitted photons by the X-ray source and the overlap of the path after several rotations is shown.

The main drawbacks of this geometry is the time consuming nature of the procedure when moving the source and detector and the partial usage of the radiation as the X-rays do not exit from the source as a pencil beam or single line.

b) Fan Beam Geometry

It is implemented to make use the lateral X-rays that the source generates. The overall shape of incident X-rays is a 2D fan that travels through a given cross-section of the object reaching to the detector. The detector can be either a row of equally spaced elements on a straight axis or equally distributed angularly on an arc shape detector (Fig. 1.15). The pair of source-detector moves in a circular way to acquire projections at all angles.

c) Cone Beam Geometry

In order to extend the fan beam geometry in 3D, cone beam CT was introduced to reduce the acquisition time and accelerate the procedure. With this type of source, a 2D detector was needed and several cross-sections are able to be imaged simultaneously. Similar to fan beam CT, the source-detector pair rotates around the object to obtain multiple views of it.

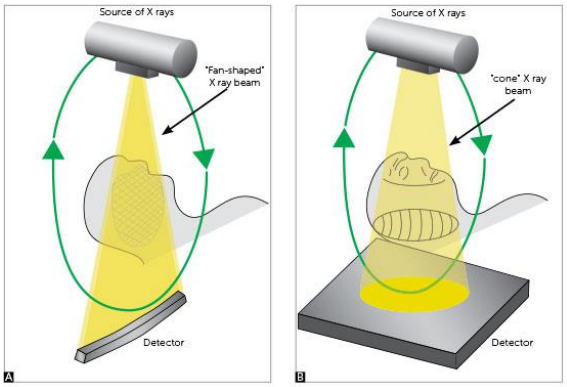

Fig. 1.15: Representation of a fan beam geometry (A) and cone beam geometry (B). Source: [7]

d) Helical Geometry

The acquisition is further accelerated with the introduction of helical movement (Fig. 1.16) of the source and the detector.

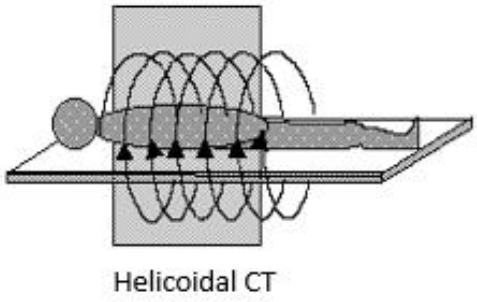

Fig. 1.16: Helical CT acquisition path scheme

While a cone-beam geometry is mostly used in preclinical CT systems, helical is the usual geometry in clinical systems.

1.3.1 Image Reconstruction

Image reconstruction is a process in which projections acquired are used to solve the 3D inverse problem so that tomographic images are obtained. There are two major categories of reconstruction methods, one based on analytical algorithms by means of a discretized physical model, and a second approach to the real solution by an iterative process.

1.3.2 Analytical Reconstruction Methods

By assuming that projections are integrals of the volume to reconstruct, analytical approaches are based on the discretization of an idealized mathematical model in the continuous space.

Taking as example a parallel beam system (Fig. 1.17), the Radon transform ($P_\theta(t)$) of a density distribution $f(x,y)$ is a 2D line integral along the anlge θ [8].

$$P_\theta(t) = \int_{(\theta,t)} f(x,y)ds = \int_{-\infty}^{\infty} f(x,y)\delta(x \cdot cos\theta + y \cdot sin\theta - t)dxdy \quad \text{(Eq. 1.6)}$$

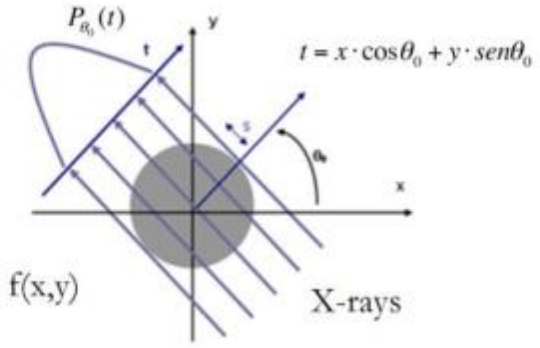

Fig. 1.17: Ilustration of the Radon transform

An inverse transformation has to be carried out to solve the equation. In order to invert the Radon transform to obtain the desired image, two different methods can be used: the ones based on the Fourier inverse transform and the ones based on Filtered Backprojection (FBP).

Fig. 1.18 shows the basis for the inversion of the Radon Transform, the central slice theorem, which states that "Fourier transform of a parallel projection of $f(x,y)$ distribution for a θ angle, is equal to the values of the 2D Fourier transform of a distribution in the line passing through the origin and forming the same angle with w axis".

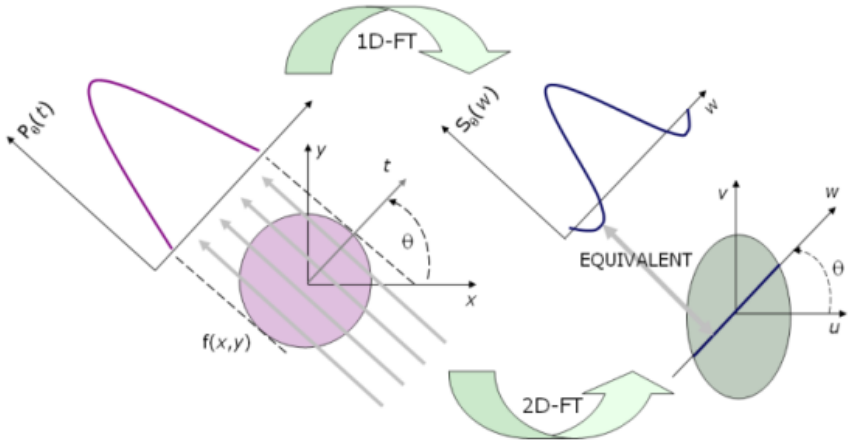

Fig. 1.18: Central Slice Theorem. Source: [8]

The Filtered Backprojection algorithm allows for the reconstruction of a two dimensional function from a set of one-dimensional projections.

Fig. 1.19 shows two simple examples to illustrate this algorithm. In the simplest case of an image matrix with only four pixels (2 x 2 matrix) two measurements for two projections will yield a system of four equations and four unknown which can be solved easily. The extension to a 3 x 3 matrix with nine unknowns can also be solved easily with twelve measured values[4]. When backprojecting the sums obtained are simply repeated back to all elements crossed.

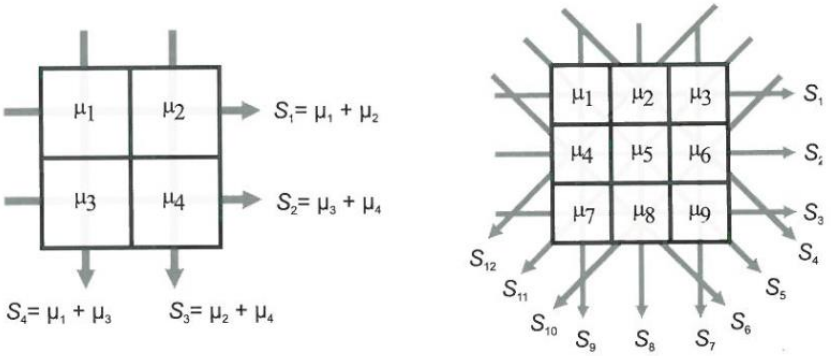

Fig. 1.19: Calculation in a NxN matrix representing the image reconstruction.

When this process is repeated for enough angles (a standard CT usually makes 360 projections around a full angular span of 360º), a blurred version of the original object can be achieved by summing up all these contributions (Fig. 1.20). With a higher number of projections the image quality is better, but the high low frequency component produces the blurring of the backprojected image.

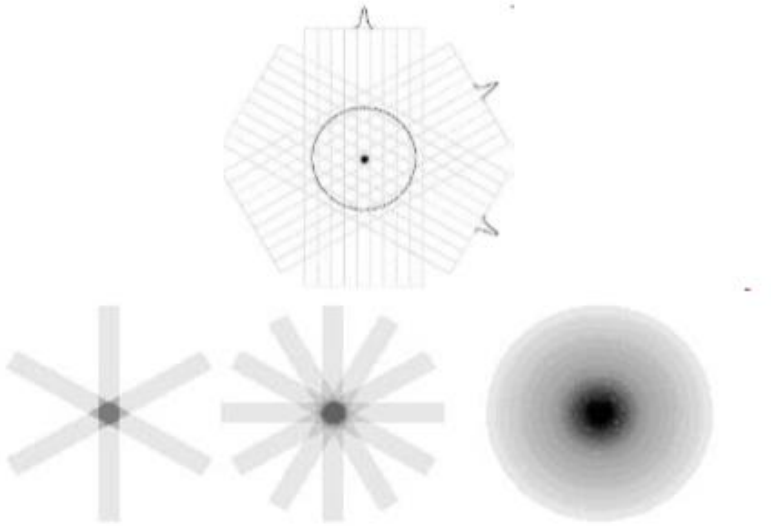

Fig. 1.20: Backprojection scheme showing the original image (top) consists of a single point. In the bottom part, images resulting from backprojection of 3, 6 and 360 degrees respectively are shown. In the last case, it can be seen how edges are smoother.

A high pass filter is needed in order to remove the excess of low frequency components that builds up and causes the characteristic blurring of the reconstructed images. In the most usual cases, a 2D ramp filter is used to enhance the edges while removing low frequencies. This is done easily in frequency domain by multiplying the blurred image to a high pass filter of same size (Fig 1.21). This back-projection method with a ramp filter incorporated is called Filtered Back Projection (FBP).

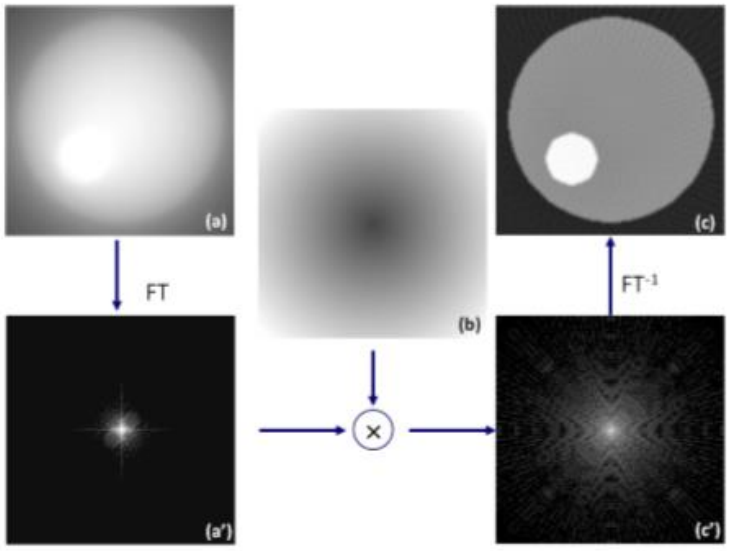

Fig. 1.21: Diagram showing a back projected image that (a) after the Fourier Transform (a') is multiplied by a 2D ramp filter (b). The result image in Fourier domain (c') is then inverse transformed back to spatial domain achieving a filtered image (c) with increased contrast resolution

In the case of a system with cone-beam geometry, the algorithm proposed by Feldkamp, Davis and Kress (FDK) is widely used [9].

1.3.3 Advanced Reconstruction

Analytical methods are considered unfeasible when the problem is ill-posed due to an incomplete set of projections acquired and advanced reconstruction methods such as iterative reconstruction are proposed [10].

The workflow of an iterative reconstruction method (Fig 1.22) starts with an estimate of the object geometry and its estimated projection is compared to those obtained experimentally (stage 1). The error image between them is then backprojected (stage 3) and this information helps to improve step by step the estimation of the reconstruction.

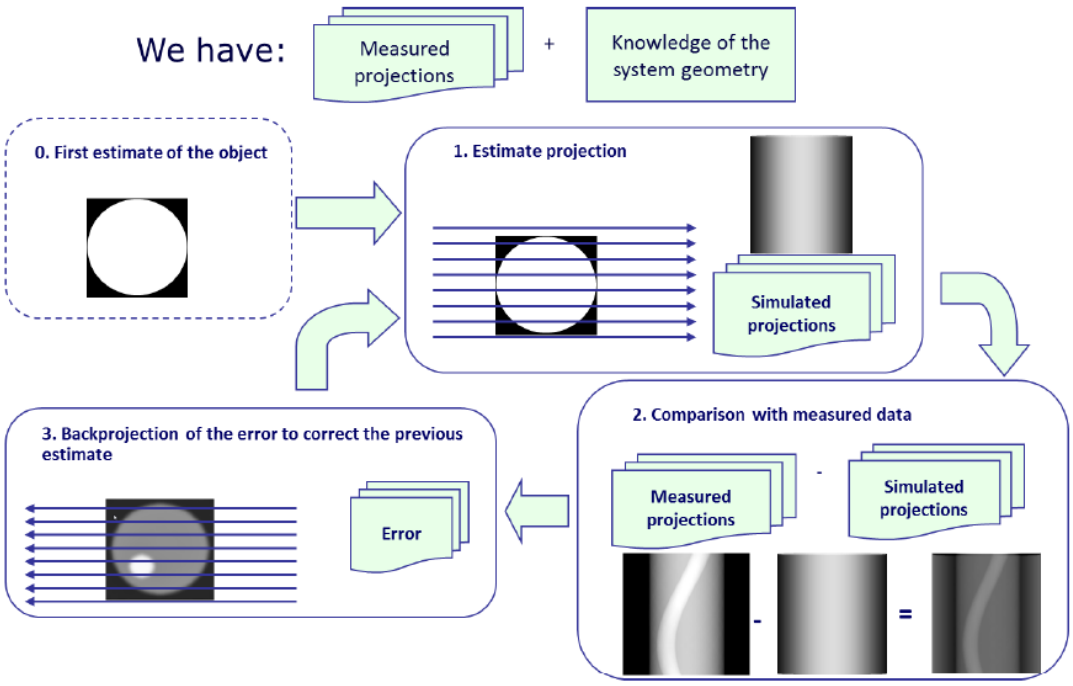

Fig. 1.22: The workflow of iterative reconstruction algorithm is represented. Source: [8]

Many iterative methods also incorporate additional known information or constrains to provide a faster convergence of the problem and obtain a more realistic estimation [11]. These prior information are usually based on the physical knowledge of the sample. The most common constrains are:

- Non-negativity condition since samples always have densities greater than zero
- Total Variation (TV) minimization. This condition imposes the homogeneity within tissues and assures their smooth and uniform appearance.
- Field Of View (FOV) constrain. The system has a fixed region of scope where the object can be seen and imaged (provided as the estimation in stage 0 of Fig. 1.22).

2 MOTIVATION

2.1 LIMITED-VIEW SCENARIOS

In a standard CT acquisition a high number of projections is obtained around the sample covering an angular range of 360º. However, there are limited-angle tomography scenarios in which only a reduced number of projections is obtained in a much lower angular span. Examples of them can be found in clinical environments such as surgery and emergency rooms or Intensive Care Units (ICUs), where life support equipment attached to the patient and surgical instruments may limit the available operating space. With the demand of real-time images and restricted space available, the imaging equipment available is usually a C-arm system that usually have up to 150º orbital coverage.

Besides, several researches have highlighted a greater risk and vulnerability of X-ray in children compared to adults for the development of a variety of tumors [12, 13]. As a CT image requires a high number of projections, the add up of dose is much greater than in conventional planar systems, making dose reduction in pediatric X-ray image an issue of special concern. Thus, it would be extremely valuable to obtain images with equivalent quality but lowering as much as possible the number of projections needed to obtain tomographic images [14-16].

However, the incompleteness of the data due to limited-view may cause aliasing and artifacts on the reconstruction. The artifacts (Fig. 2.1) are revealed as streaks extending from the center of rotation and deteriorates brutally the image quality [17]. The problem is even worsened when small details are required since they contribute as high frequencies in the Fourier domain and, according to Nyquist Law, the sampling frequency has to be at least the twice of it.

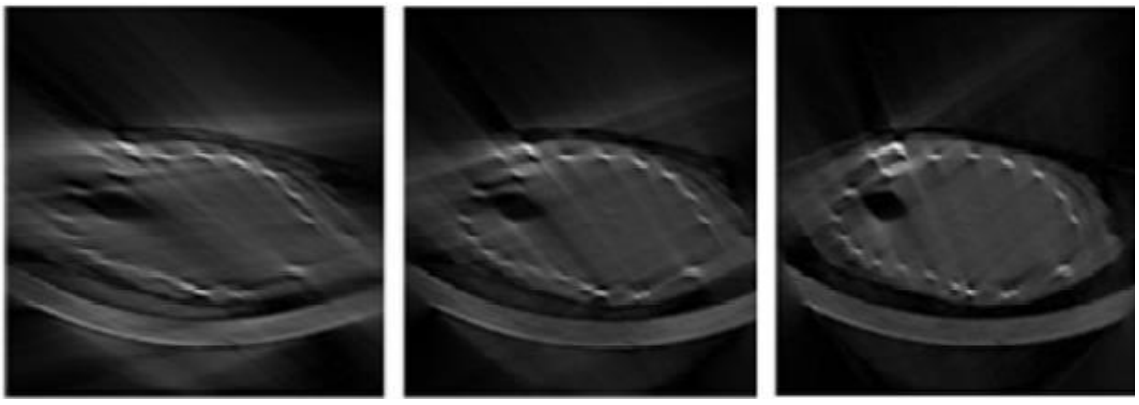

Fig. 2.1: Artifacts derived from FDK(cone beam back-projection algorithm) with 60º (left), 90º (center) and 130º span angles.

It is worth mentioning that aside from the resolution loss, the diagnostic capacity is maintained as long as a minimum number of projections is ensured. In recent years, a large number of studies have been conducted trying to solve the challenge of limited-data in CT reconstruction[11, 18]. Due to the incompleteness in Radon domain, it was

widely believed that a reconstruction based on less than 180 projections would not be able to generate images with an acceptable quality.

The growth of research on iterative reconstruction methods enables the chance to accomplish an artifact-free CT image from a set of limited projection data. As explained in the previous section, prior information has been proposed to compensate the lack of data.

2.2 CONTEXT

This bachelor thesis is framed on one of the lines of research carried out by the Biomedical Imaging and Instrumentation Group (BiiG) from the Bioengineering and Aerospace Department of Universidad Carlos III de Madrid working jointly with the Hospital General Universitario Gregorio Marañón (HGUGM) through its Instituto de Investigación Sanitaria. This line of research is carried out in collaboration with the company Sociedad Española de Electromedicina y Calidad (SEDECAL) which opens the possibility to achieve the transfer of technology to the industry.

A previous work developed by BiiG group, presented the possibilities of limited view tomography with a novel iterative method, the Surface Constrained method for Limited-Data Tomography (SCoLD)[19]. This proposed method is based on the incorporation of the exact geometrical surface information to compensate the lack of data in limited-view scenarios where a few projections are acquired in a reduced angular span. SCoLD restricts the space of search considerably with the surface-based support helping to converge to a better solution. The study showed that SCoLD allows to restore the altered contour of the sample and suppress greatly the streak artifacts. However, it was only carried out by simulations using a surface mask extracted by thresholding and morphological operations of a reference CT. However, its experimental application including the surface extraction has not been probed yet.

2.3 OBJECTIVES

The overall objective of this thesis is the evaluation of the SCoLD method with real data. This general objective can be detail in the following challenges:

1) Evaluate the general applicability of different 3D scanning technologies available in the market for its application in medical imaging. The management of a 3D scanner in clinical/pre-clinical environment needs to be adapted as it differs from the usual operating spaces.

2) Design a complete workflow to obtain surface information from real data. The transformation of the outcome into a usable format in tomographic reconstruction algorithms must be implemented.

3) Evaluate the results obtained with the proposed workflow. Obtaining of proper iterative reconstruction results with the SCoLD method is highly dependent on the parameters and information provided so that an optimization procedure is likely to be required.

2.4 OUTLINE OF THE MANUSCRIPT

The following chapters are included in the manuscript:

- Chapter 1: Introduction. This chapter describes a theoretical background on X-ray imaging. Differences between planar X-ray and CT are described together with the concepts of projection and the reconstruction.

- Chapter 2: Motivation. This chapter introduces the line of research in which this thesis is included and the specific objectives of this work. Context and socioeconomic environment are described.

- Chapter 3: 3D Scanners. This chapter describes currently available technologies in 3D scanners, analyzes the technical requirement for the application proposed in this work and summarizes a comparison among few commercial options.

- Chapter 4: Proposed method. This chapter presents a complete workflow to obtain surface information from real data and the processing required to transform it into a suitable format for tomographic reconstruction algorithms.

- Chapter 5: Evaluation. This chapter describes the methodology used for the evaluation of the method proposed in Chapter 3 with real data.

- Chapter 6: Results.

- Chapter 7: Discussions and future works.

- Chapter 8: Project management

2.5 REGULATORY FRAMEWORKS AND SOCIOECONOMIC ENVIRONMENT

Experimental practices with animal as well as their housing and care done for this work are accomplished in accordance with the legislation (Real Decreto 53/2013 º(39) and 86/609/EEC), of animal protection applied in Unidad de Medicina y Cirugía Experimental (UMCE) of Hospital General Universitario Gregorio Marañón (HGUGM) and are permitted by the Animal Experimentation Ethics Committee of HGUGM.

The three “Rs” rule introduced by W.M.S. Russel were taken into account when designing the experiments *in vivo*:

- **Replacement:** The use of living animals for the testing is avoided unless necessary.
- **Reduction:** The number of animals used is kept as low as possible and studies ae not repeated avoidably.
- **Refinement:** The impact of any procedure should be as small as possible.

The application of the results obtained in this thesis in novel radiography systems brings the opportunity of obtaining tomographic images while maintaining the radiation dose very low compared to CT systems. The impact on the clinics may include:

- The increase of image information would avoid the need of additional exhaustive exams optimizing the efficiency of Radiology Department.
- This technology may increase the role of radiographic systems, which accounts already for the 80% of the medical imaging studies performed in the clinics.
- This technology could enable obtaining 3D images where a conventional CT system is not available due to limitations of mobility of the patient or restricted accessibility for a CT equipment such as ICU or during surgery.

Finally, it would bring the possibility of advanced techniques in underdeveloped countries or rural areas, by providing tomographic images with a lower cost than a CT. The transfer of this technology to SEDECAL will benefit the national industry assuring its leadership in such a dynamic sector, by including the newest imaging tools into their radiology systems.

3 3D SCANNERS

A 3D scanner is a device that analyses a real-world object or environment to collect data on its shape and possibly its appearance (e.g. colour). The collected data can then be used to construct digital three-dimensional models.

Direct measuring methods are used to measure the magnitude or recover the 3D geometrical information of a real object. These methods are especially easy if the objects are constructed by basic shapes, however, real objects do not have a uniform geometry. Recent developments enable mimicking the depth perception of the human eyes using two or more cameras, thus determining the distance of a point cloud given by the object and estimate the whole external geometry by generating vertices among them.

Applications of 3D scanners may include industrial design, quality control and prototyping, model construction for 3D printing and digitization of art gadgets among others [20]. Many different technologies can be used nowadays to build these 3D-scanning devices. Some of them are described below.

3.1 CONTACT 3D SCANNERS

These scanners work by touching the scanning object (Fig. 3.1). The object must be laying on a flat, fixed surface to avoid movements and the scanner is usually a moving arm maps the distance calculated when reaching the object surface. This type of scanner can be very precise for the distance obtaining therefore mostly used in the manufacture of precision required pieces and quality controls. Another advantage of this technology is that it can be applied to a reflective or transparent object as there is no light involved. However, the force applied onto the object surface may cause deformations when it is not completely rigid and thus possible damages take place. Time requirement is also a main limitation as a large acquisition time is spent to move physically the arm.

Fig. 3.1: A coordinate measuring machine (CMM)is shown as an example of contact based 3D scanner.

3.2 NON-CONTACT 3D SCANNERS

a) Time-of-Flight

A scanner based on time-on-flight principle emits a pulse signal of laser and processes the time it took to bounce back after strike to the object surface (Fig. 3.2). Since the speed of light is known, the time spent in the trip can be easily calculated and thus the distance from the sensor to the reflecting surface can be determined. Both the scanner and the object should be fixed and hold stable on the place as it measures one point at a time. The entire region desired needs to be scoped by either rotating the whole setup or diverging the laser pulse by mirrors. The precision of these devices is mainly dependent on the accuracy of the time sensors and due to the fast nature of lasers, the time precision is limited. On the other hand, thanks to this property, this device is made more suitable for the measurement of geographic features or large goods.

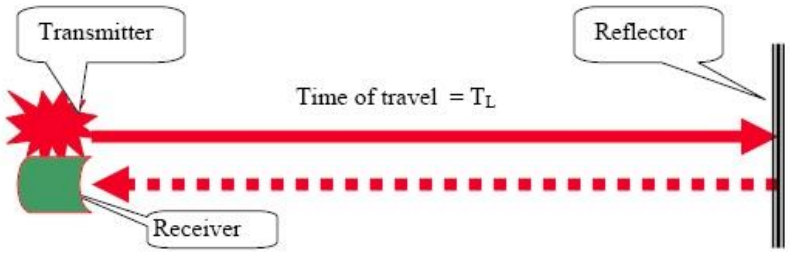

Fig. 3.2: Example scheme showing the working principle of a time-of-flight scanner, the laser/transmitter shines on the target/reflector while the sensor/receiver detects the reflected light.

b) Triangulation

Similar to the previous technique, triangulation based scanners detects the pulse of a laser emitted, but it looks for the laser dot inside the FOV of a camera instead of the round-trip time (Fig. 3.3). The name of this setup comes from the triangle form by the three elements: the laser dot, camera and the emitter. Triangulation scanners are intended for the acquisition of small objects at a closer distance and its accuracy is significantly higher than a simple time-of-flight based device.

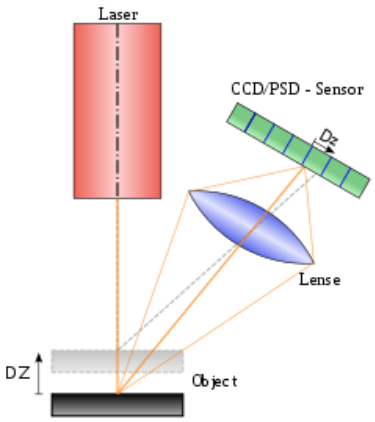

Fig. 3.3: Working principle of a triangulation scanner where CCD stands for charge-coupled device.

c) Conoscopic Holography

A conoscopic holography device (Fig. 3.4) emits a laser source towards the surface of the target. When the laser beam is reflected back along the same path, it is projected onto a CCD (Charge-Coupled Device) and detected as a diffraction pattern. This will be transformed in frequency domain allowing to determine the distance to the surface. Advantages have been seen when using these devices to scan cavities and this is the reason for researches conducted for its application on computer assisted surgery with a multi-camera optical tracking system.

Fig. 3.4: Example of a conoscopic system: ConoProbe. Source: [21]

d) Structured Light

Instead of using a point source, structured light based scanners emit a light pattern and analyzes it deformation after strike on the target (Fig 3.5). The advantage to highlight in these devices is the speed of acquisition as a large number of points can be captured for the calculation of the distances at the same time. Moreover, many portable commercial options have been launched already making easier their adaption in clinical environment and avoid the installation of needed accessories.

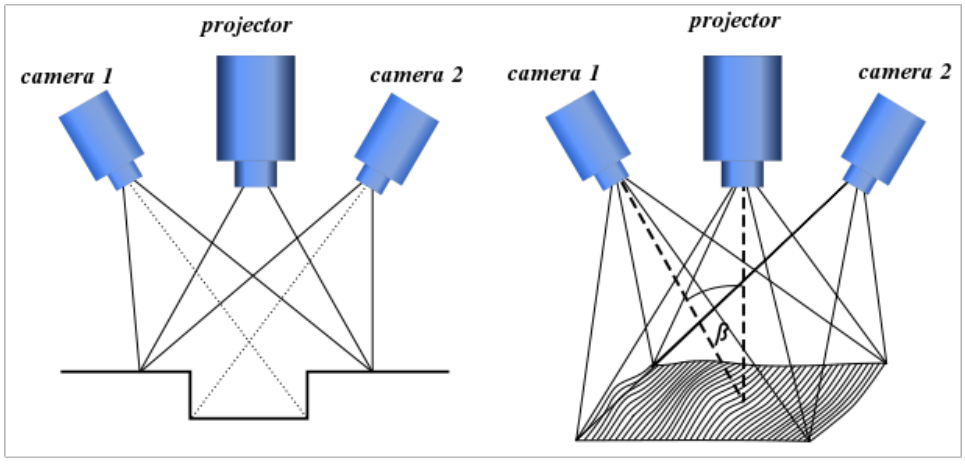

Fig. 3.5: A schematic representation of a structured light scanner recording system. The projector emits the light pattern and the pair of cameras records the distortion at two different angles to prevent obstructions.

As all other light based scanners, difficulties are seen when the surface desired is transparent or reflective. These properties of the material cause the light to be over-reflected outside the current scanning area or almost no light is reflected for the detection.

3.3 SELECTED SCANNER

Among the available 3D scanning technologies, we considered that non-contact structured light scanners are the most suitable for an easy setup in a clinical or preclinical environment. In these scenarios the space is shared by many devices or equipment, so the scanner must be easy to handle, apart from allow a fast scanning process since we are dealing with living organisms and it is required they remain immobile.

Table 3.1. shows a summary of the available scanners based on structured light:

3D SCANNER	TEXTURE	ESTIMATED PRICE (€)	MAXIMUM RESOLUTION (MM)	MAXIMUM ACCURACY (MM)	ACQUISITION SPEED (POINTS/S)	WORKING RANGE (M)	WEIGHT (KG)
ARTEC EVA	YES	14K	0.5	0.1	2 000 000	0.4 - 1	0.85
CREAFORM GO!SCAN	YES	25K	0.5	0.1	550 000	0.4 - 0.65	0.95
PEEL3D 3D SCANNER	NO	5K	0.5	0.25	550	0.4	0.85
VIALUX ZSNAPPER PORTABLE	NO	15K	0.1	0.1	-	-	2.3
THOR 3D DRAKE	YES	13.5K	0.15	0.03	1 200 000	0.4 - 1	2.3

Table 3.1 Comparison of some options for handheld structured light based 3D scanners on the market.

The *Artec Eva* (Fig. 3.6) was chosen for the study of the limited-view problem due to its significant faster acquisition speed and its versatile working range. Another reason for this selection is its availability in the group, where it has been used for image guided surgery. Its applicability on body scanning has already been reported for a wide range of clinical usages [22].

Fig. 3.6: 3D scanner Artec Eva

4 PROPOSED METHOD

In this chapter we present a complete protocol for obtaining a 3D image from limited-view tomographic data (Fig. 4.1). We propose the use of a 3D structured light scanner to extract information about the contour of the sample in order to have prior information to compensate the lack of data and solve the reconstruction problem.

While a standard procedure involves exclusively a FDK reconstruction of the projections, we have introduced additional steps to obtain prior information about the sample geometry using the scanner *Artec Eva*. The surface mask generated is used for an advanced reconstruction method so a registration procedure is needed to align it with a preliminary reconstructed volume. To facilitate the registration process we placed some makers on the sample before the acquisition.

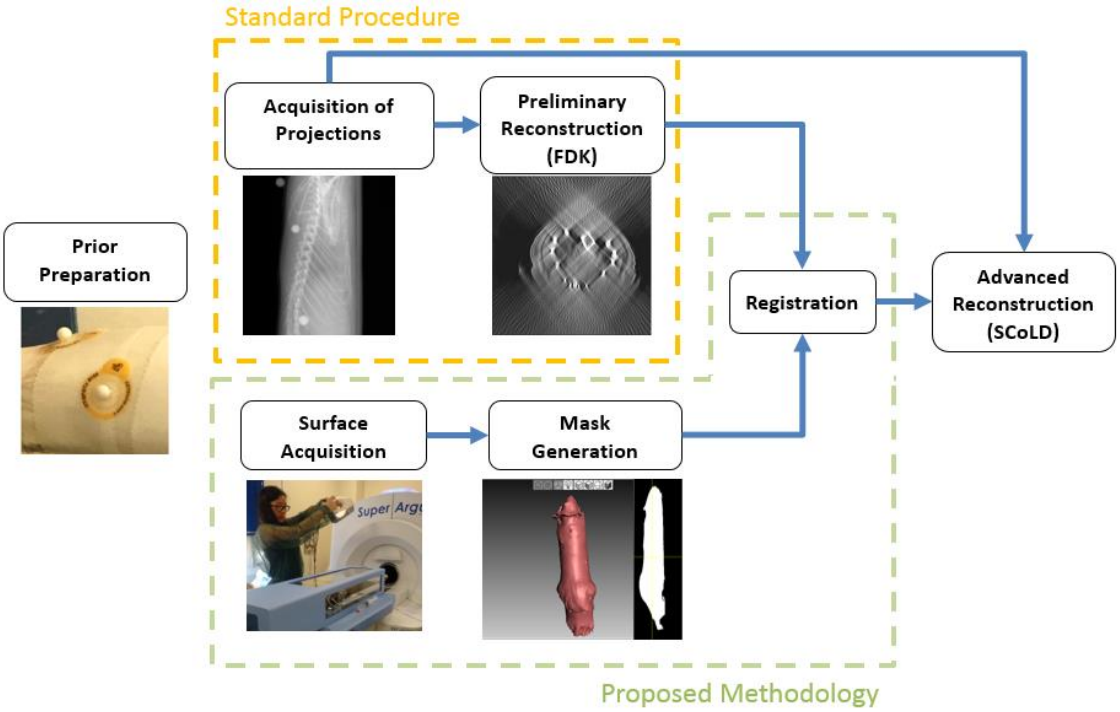

Fig. 4.1: Scheme describing the complete workflow of the proposed procedures.

The following sections of this chapter describe the main issues of the proposed workflow showing examples of the data generated in each of them.

4.1 DATA ACQUISITION

The procedure starts with the preparation of the sample and the background that is crucial for the surface acquisition with the structured light scanner.

On the one hand, to facilitate the detection with the light scanner, an even, brighter surface of the object is preferred. We used tapes or tights to uniform the hair of the animal and placed the markers on top of them so that they are better identified in the surface

mask (Fig. 4.2). On the other hand, an irregular background helps the scanner to keep the track. The acquisition table, for example, was covered by fabric to create a bumpy appearance.

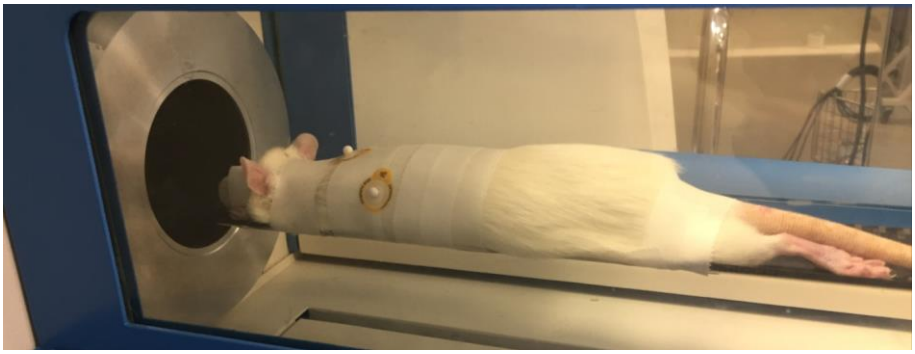

Fig. 4.2: Example of preparation of the samplewith white tapes surrounding the thorax of the rodent and the bed to smooth the irregular hair texture of the sample

Markers (Fig. 4.3) are used as landmarks for the registration process. We used 3 spherical ceramic-based markers with a diameter of 4 mm in order to allow its visualization with the light scanner but avoid causing significant artifacts in the CT images. They were placed separated from each other as much as possible without exceeding the FOV of the detector for all projections.

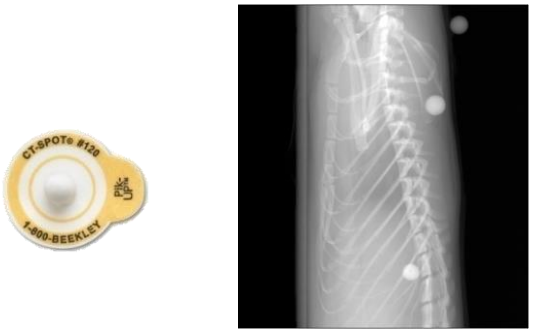

Fig. 4.3: Marker used in the study(left) and an example of its visualization in projection (right).

For the standard CT reconstruction (based on the FDK algorithm) we used the software Mangoose [23, 24] developed by the BiiG group in association with Computer Architecture and Technology Area (ARCOS) group, both from UC3M.

4.2 Surface Acquisition and Mask Generation

The structured light scanner *Artec Eva* is associated with its own software *Artec Studio* that provides a user interface composed of several panels with a wide range of tools (Fig. 4.4).

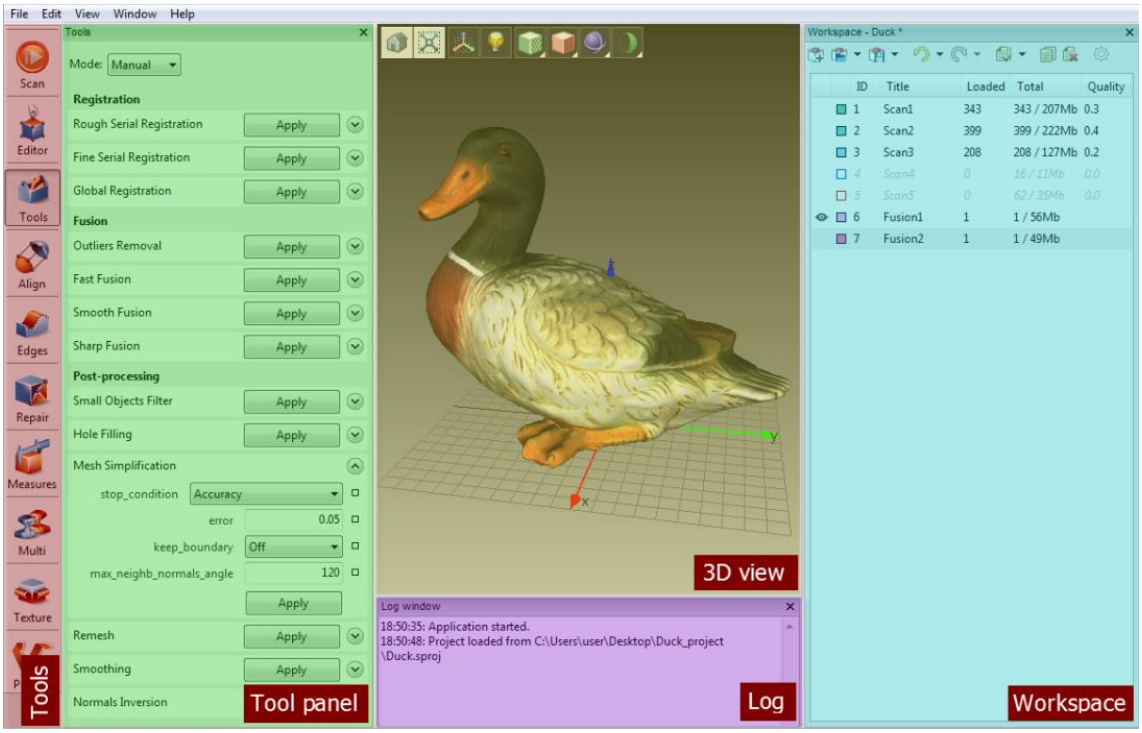

Fig. 4.4: Components and the default layout of *Artec Studio*

In the next subsections details are given for every step needed to successfully generate a surface mask using the light scanner.

4.2.1 Data Acquisition

Before starting the acquisition process, a *preview mode* allows to adjust several parameters such as texture *brightness*, *sensitivity* or *frames per second* (fps, number of "photographs" of light pattern made each second) depending on the working conditions and the scanning mode we use (Fig. 4.5). Once the object can be properly seen, the acquisition starts.

The software uses the concept of "Project" for the set of scans generated during the whole acquisition. Each scan represents a part of the sample and is created after pauses and loss of focus (hereinafter referred to as "tracking loss"). In turn, each scan is composed of a sequence of frames.

The acquisition mode chosen was *Real-time fusion* (Fig. 4.6) since it allows visualizing the merged scans while the collection of the data.

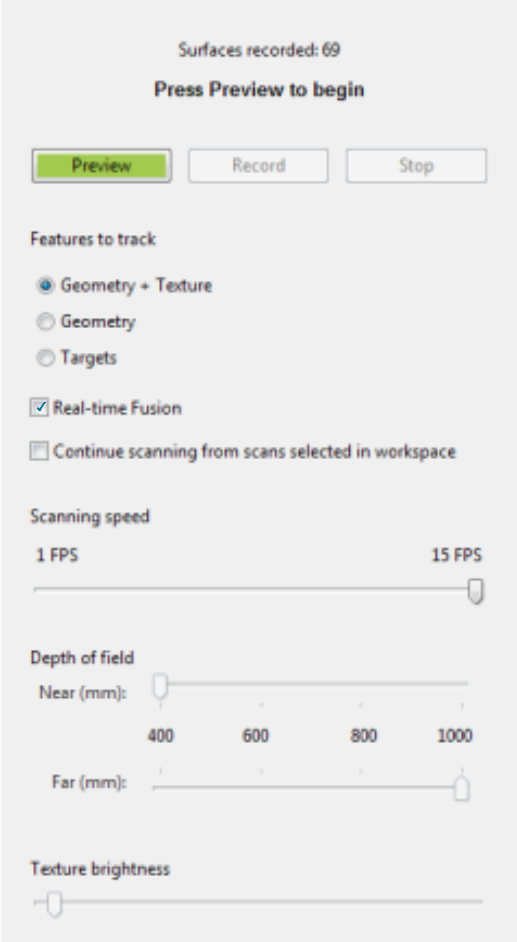

Fig. 4.5: Presetting parameters to be adjusted before the acquisition.

The distance from the scanner to the object and the orientation of the scanner is adjusted to scan the sample from different angles to covering the complete surface (Fig. 4.6). The interface gives information about distances by means of a histogram and green lines over the scene which help to know what area is being focused (Fig. 4.7). The movement of the scanner needed to be done gently to avoid the tracking loss. The process is stopped when the sample to scan is seen completely.

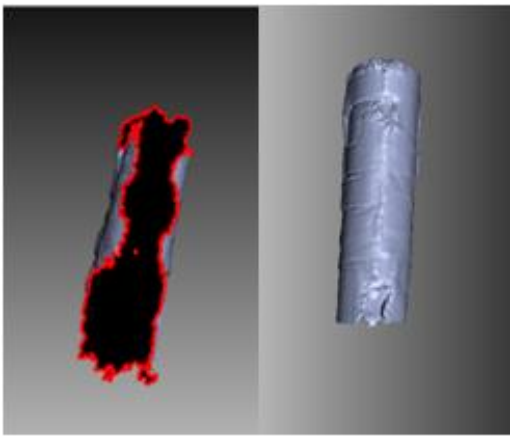

Fig. 4.6: (Left) The geometry of the sample with a hole due to uncovered views. (Right) Complete geometry after a complete acquisition process.

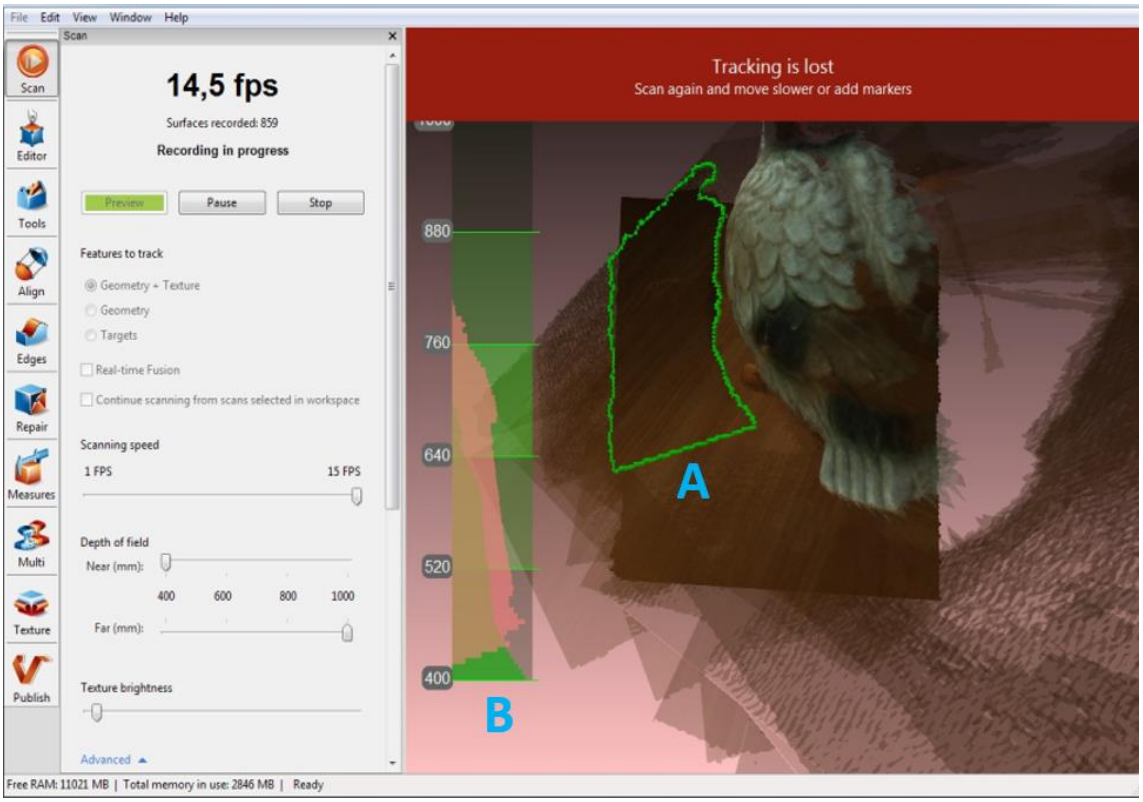

Fig. 4.7: Example scenario of scanning and tracking lost situation.Green lines near to the object shows the focused area (A) while in the range meter (B) we can see that current position (green histogram) does not match the previous one (red histogram).

4.2.2 Data Processing

In order to successfully incorporate the data acquired in an advanced reconstruction algorithm, it has to be processed and converted into a suitable data type. As tracking loss is common during acquisition, the fusion of several scans is required to obtain a unique surface model. Besides, structures that do not belong to the sample must be eliminated, while missing parts must be modelled.

This process can be done automatically by the option *real-time fusion* or manually. Fig. 4.8 shows a scheme of the tools used in each option. While the *real-time fusion* starts directly with *Eraser,* a manual fusion requires further steps to create a *smooth fusion.* Both methods involve common steps to improve the fusion created.

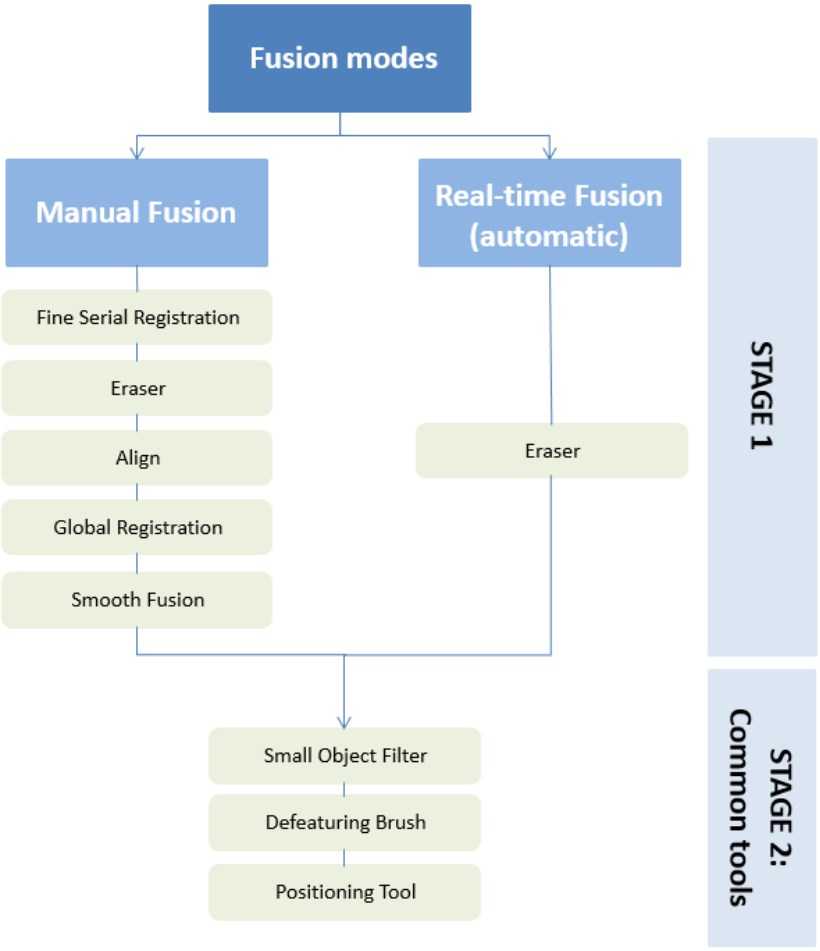

Fig. 4.8: Processing tools to create a unique surface model from different scans.

The reason to use a manual fusion instead of the *real-time fusion* is that the later may sometimes fail to represent fine details successfully or extrapolate the uncovered views. The manually option allows the user to adapt the model for specific features of interest. (Fig. 4.9).

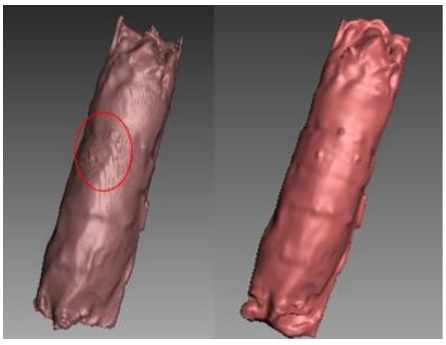

Fig. 4.9: Example of the aspect of markers after a poor *real-time fusion* with the automatic option (left) and its equivalent with the manual option (right).

The first step is to review individually each scan. Scans with no useful information are eliminated while the rest are processed to create the surface model. Then, we check the result of the *real-time fusion.* If the result is appropriate, only *Eraser* is applied in Stage 1 eliminating unwanted elements and the processing continues with Stage 2. In the

cases in which the manual fusion is required for the first stage, the following tools are used:

1. *Fine Serial Registration* performs an automatic correction on frames that are captured in each individual scan to avoid possible misalignments between frames.

2. *Eraser* eliminates for each scan the surroundings that are not needed. The aim of this step is to remove big unneeded portions (Fig. 4.10) such as the background. A good preliminary preparation of the environment as described in 4.1 allows having the sample and the background easily separable in different planes facilitating the deletion in this step.

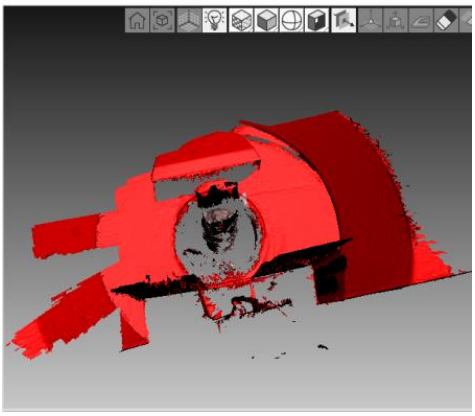

Fig. 4.10: Example of background removal using *Eraser* tool. The region to be erased is represented in red

3. *Align* tool is used to align a series of scans. Usually different scans present different orientations so that it is necessary to align them in the same coordinate system. Once more, this tools can be performed both manual (Fig. 4.11) or automatically. In a manual manner, pairs of markers are placed in points of interest shared between a reference scan and the rest of the scans.

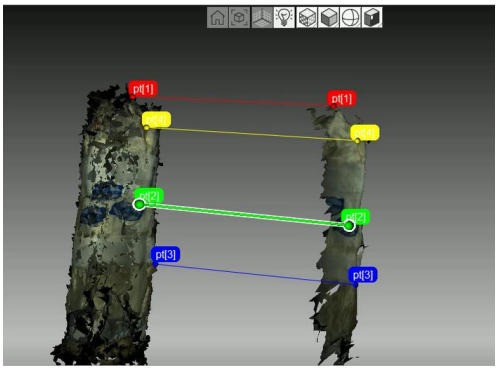

Fig. 4.11: Manual alignment of scans

4. *Global Registration* is used to adjust the texture information between scans. This step gave a cleaner look of the shape and texture of the sample and improved considerably the resolution of the frames. After this step, frames with redundant information inside the same scan can be identified and erased.

5. *Smooth fusion* merges the scans and fills the holes due to missed views. This was especially useful for spaces at inaccessible views, such as those under the bed of the CT equipment (Fig. 4.12).

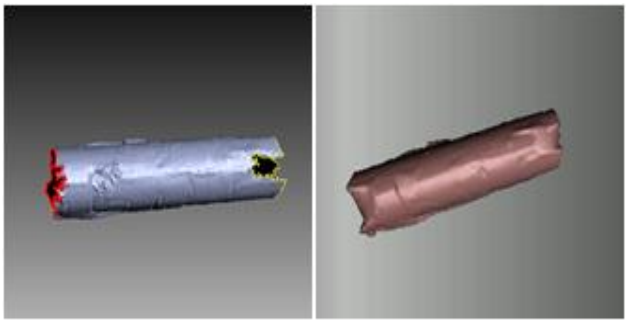

Fig. 4.12: (Left) Holes (in red and yellow) are filled (right) using *Smooth fusion*.

The common tools for the second stage are:

1. *Small object filter* removes the small objects not connected to the sample. This step can be also applied before step 5 to clear all small fractions that may affect to the result of the fusion.
2. *Defeaturing brush* and other *editing tools* are used if there were still some structures to be smoothed.
3. *Positioning tools* are used to rotate, move and place the object in the desired orientation.

Finally, the model generated after these steps is exported as a STL mesh.

4.2.3 Voxelization

The mesh exported from Artec Studio in STL format is a collection of vertices and faces that define polygons that represent the 3D object (Fig. 4.13). With the help of the source code *polygon2voxel* [25] implemented in MATLAB (The MathWorks Inc., Natick, MA, USA), we transform the polygon mesh into a volume of voxels using the following inputs:

- The size of the corresponding volume (X, Y, Z). X and Y corresponds to axial dimensions of the CT volume while Z is set larger to cover the whole sample.
- A scaling matrix to resize the voxel size to the one of reconstructed volume.

The result is a volume containing the 3D mask in which the value of “1” is assigned for the surface of the sample and “0” for the background

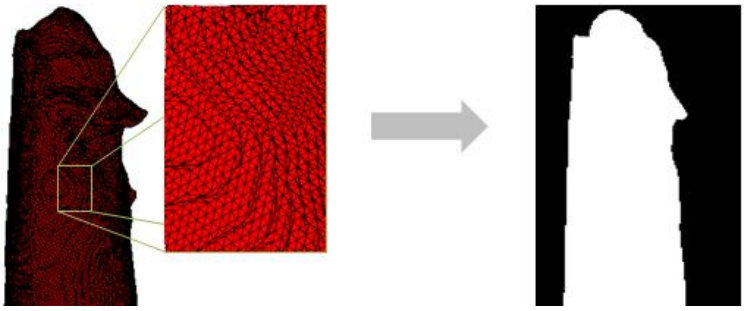

Fig. 4.13: The polygon mesh of the surface (left) is converted into a volumetric binary mask (right).

4.3 REGISTRATION

Since the scan was made along the whole body of the rodent, the binary surface mask generated has to be adapted to the FOV acquired in the CT volume. Moreover, the CT volume and the surface volume present different coordinate systems, thus requiring a registration process to align both volumes (Fig. 4.14). A rough cut is made first around the interest region to make the amount of data manageable and reduce the computational cost of the software.

Then, we use the image processing and visualization software *3d Slicer* to perform the registration taking the markers attached to the skin of the animal as reference points.

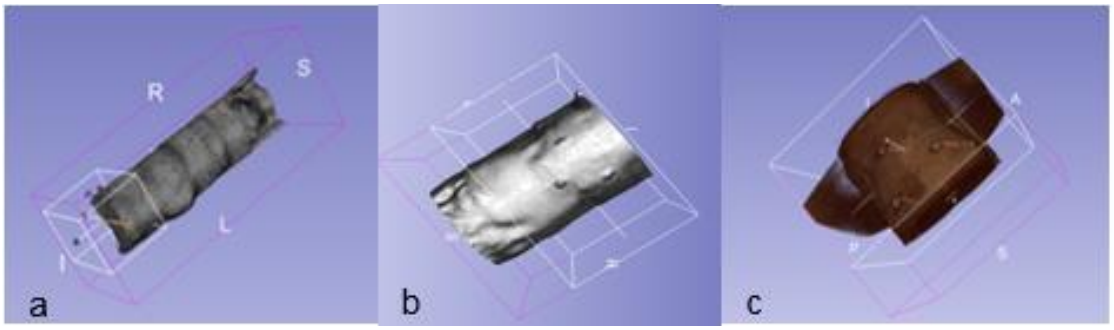

Fig. 4.14: 3D visualization of the entire mask generated(a); a rough approximation to the FOV of the CT study (b); volume rendering of the CT volume (c).

The detailed workflow followed in *3d Slicer* is:

1. The M*arkups tool* is used to:
    a. Establish fiducial points in the CT volume (Fig.4.15). We set one in each of the three markers that were placed over the sample. These fiducials points were fixed as *reference points*.

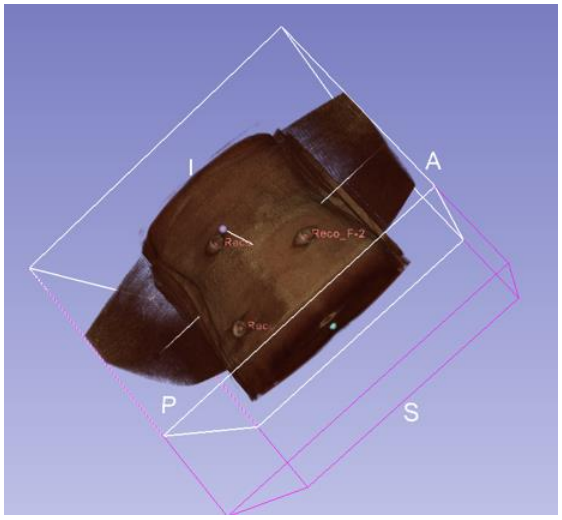

Fig. 4.15: Placement of fiducials seen as red dots at the centroid of the spherical markers

    b. Place another set of fiducials in the volume of the surface mask (Fig. 4.16). The markers here are not perfectly spherical and the accuracy of the placement depends on the user experience. These fiducials are the

ones to bring into the coordinate system of the *reference points*, and are usually known as *moving points* in registration softwares.

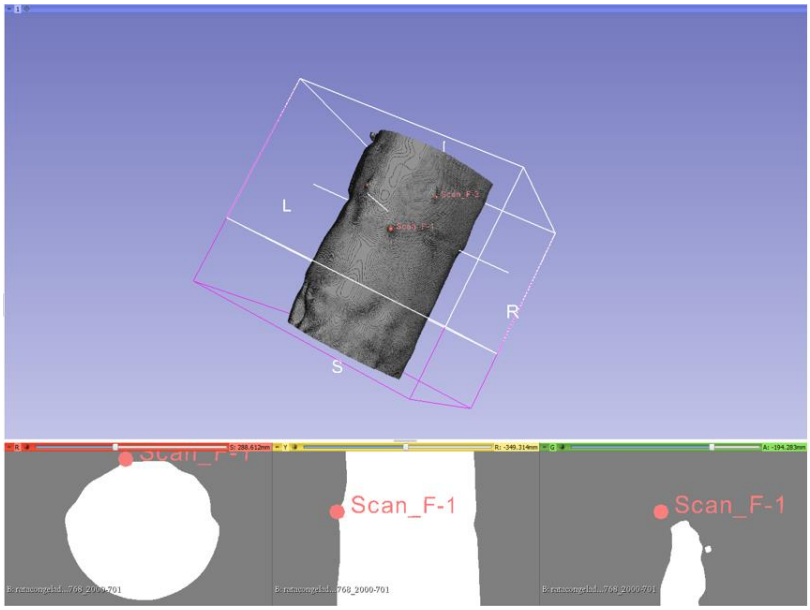

Fig. 4.16: Distribution of the fiducial points(red dots) on the binary mask. At the bottom the three anatomical views showing the fiducial points.

2. We use the module *Fiducial Registration* to calculate the rigid transformation that matches the coordinates of the *moving points* with the *reference points* (Fig. 4.17). The near distribution of the markers over the animal due to the limitation of the FOV may cause them appear in close planes in the model. This together with manual uncertainties in positioning may sometimes cause errors when computing the transformation. In these cases, further adjustments can be done with the *Transforms* module.

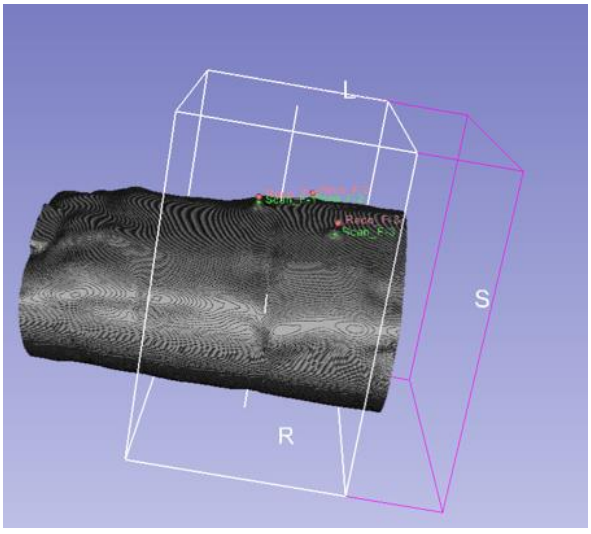

Fig. 4.17: Result of the alignment where both sets of fiducials overlap.

3. With the transformation obtained, we use the module *Resample Scalar/Vector /DWI Volume to* apply the transformation computed and resize the surface mask taking as reference the CT volume (Fig. 4.18).

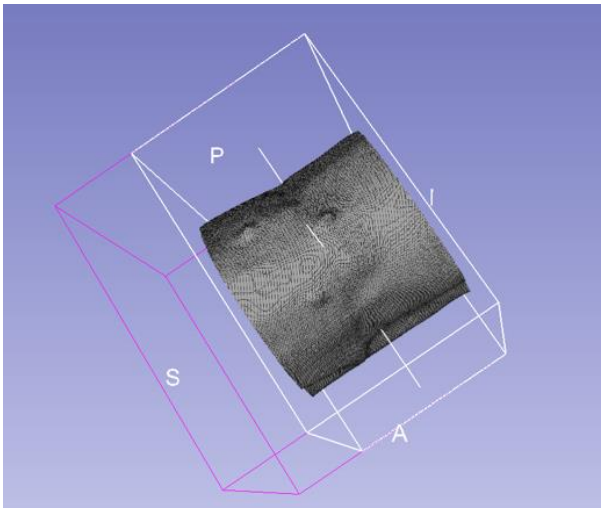

Fig. 4.18: The final output volume obtained.

At the end of this stage, a subvolume of the surface mask with the same orientation and the same anatomical region as CT volume is obtained.

4.4 ADVANCED RECONSTRUCTION

Once the mask is aligned with the FDK volume, the limited-data is reconstructed using the SCoLD [19] method, which makes use of the surface mask as prior information. This algorithm has been implemented using the projection and backprojection kernels developed in the simulation framework, FUX-Sim [26], developed also by the BiiG group.

The method is based on the mathematical equation of an iterative problem through TV minimization and non-negativity condition:

$$\min_{u} \quad \|\nabla \mathrm{u}\|_1 \quad \text{s.t.} \quad \|\mathrm{Au} - \mathrm{f}\|_2^2 < \sigma^2, u \geq 0, u \ \epsilon \ \Omega_s \qquad \text{(Eq. 4.1)}$$

where u is the reconstructed image, A is the system matrix, f is the acquisition data and σ^2 is the image noise, Ω_s corresponds to the surface support. The method aims to find an optimum u that satisfies that the difference between the estimation and the data should be lower than the intrinsic data noise.

The problem (Eq. 4.1) is solved using the Split Bregman formulation[27] that allows to reduce the optimization problem into several simpler sub-problems that are solved iteratively. It also allows to separate the TV term to solve it in a different way because it is not differentiable. Based on these derivations, the SCoLD method imposed the surface constraint that restricts the space of search resulting in a better convergence rate and image quality.

Several parameters of the method associated with the different assumptions should be optimized because they affect the final image quality:

k: Number of iterations. This parameter should be large enough to assure the convergence.

α: This parameter controls when the details and edges information start to be included in the intermediate solutions of u.

γ: This parameter weights the surface constraint and should be lower than 0.1

μ: This parameter weights the data fidelity term. Higher values result in faster convergence of the method.

λ: This parameter weights the Total Variation assumption, which affects the smoothness of the resulted image.

5 EVALUATION

The evaluation of the previously proposed protocol is done in a rodent study. To study the viability of the method, the results obtained from a limited-view scenario are compared with those obtained from a standard micro-CT study. In addition, the feasibility of using the proposed surface scanner (*Artec Eva*) to obtain information about the surface of the sample is studied.

5.1 CT DATA

A standard CT of 360 projections over an angular range of 360 degrees was acquired with the preclinical CT equipment SuperArgus PET/CT, commercialized by SEDECAL. The current and voltage of the source were set at 340 µA and 45 keV, respectively. The size of the projections was 516x574 pixels with a pixel size of 0.2 mm. From this complete set of 360 projections, we selected only 120 projections over an angular range of 120º in order to evaluate the scenario of limited-view.

Both the standard CT and the limited-angle CT were reconstructed with Mangoose generating two volumes with a matrix size of 516x516x574 pixels and a voxel size of 0.122 mm. Figure 5.1 shows an example of the reconstructed volumes. The result from the standard CT is considered the *gold standard*. The reconstruction from the limited data corresponds to the preliminary reconstruction used for the registration step with the surface of the sample.

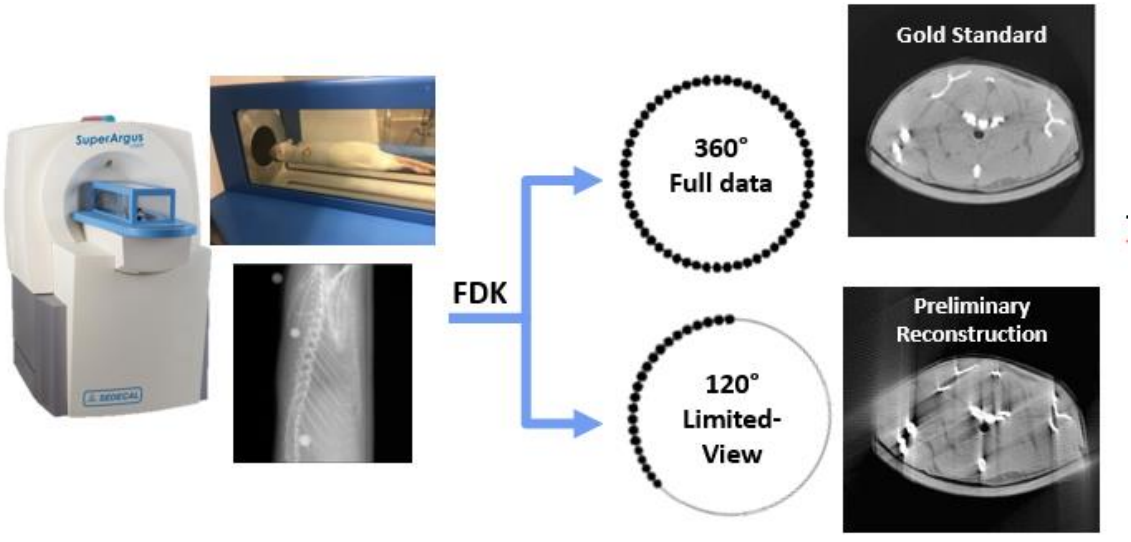

Fig. 5.1: Scheme of real CT data evaluation

5.2 SURFACE MASK

An ideal mask was generated from the standard CT reconstruction by thresholding using the image processing tools in ImageJ (Fig. 5.2). We filled the holes and applied morphological processing (opening) to remove small alterations (mainly due to hair layer distortions).

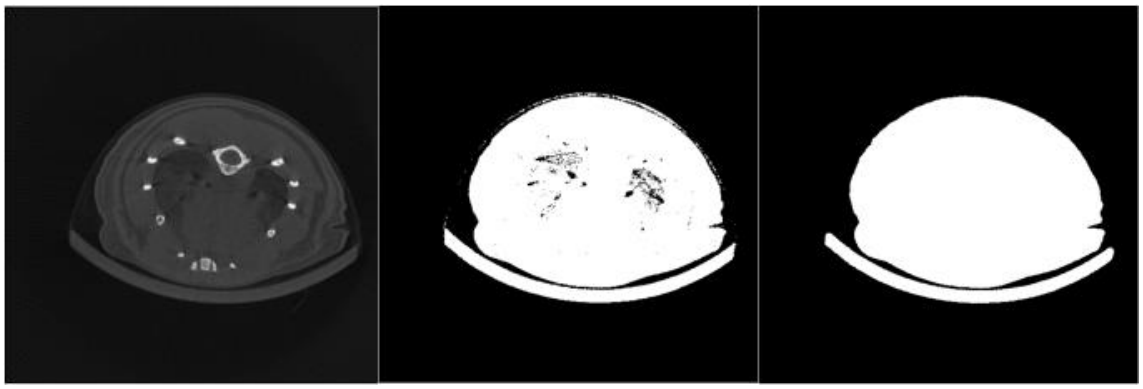

Fig. 5.2: Ideal reconstruction with FDK algorithm using a complete set of data (left), ideal mask obtained by thresholding (middle) and the final ideal mask after opening and hole filling (right).

The surface of the rodent was acquired with the scanner Artec Eva, processed following the steps described in the previous chapter (Fig. 5.3) and converted into a binary mask (Fig. 5.4) using the scaling factor $\frac{1}{0.122} \approx 8.2$. From now on this mask will be referred as *real mask*.

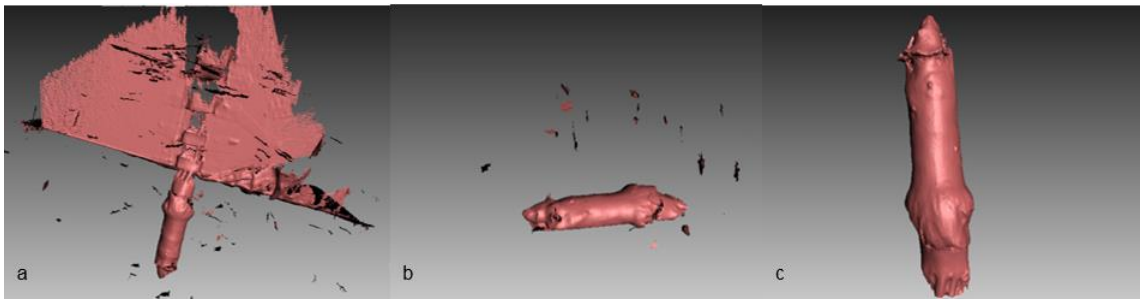

Fig. 5.3: Surface processing steps: a) Surface model without background removal. b) After background removal, small objects can be further cleaned. c) Final surface model exported.

Fig. 5.4: Binary 3D mask obtained from the surface model: a) coronal view, b) axial view and c) sagittal view.

In order to quantify the similarity between the real and the ideal masks, the Sørensen–Dice coefficient is calculated. This statistic gives a quantitative estimation of the difference between two samples (Eq. 5.1). A Dice coefficient of 1 means the greatest similarity with both masks being identical in terms of area occupied, while 0 means that no overlap has been found[28].

$$Dice\ Similarity\ Coefficient\ (DSC) = \frac{2|Ideal\ mask \cap Surface\ mask|}{|Ideal\ mask| + |Surface\ mask|} \quad \text{(Eq. 5.1)}$$

5.3 ADVANCED RECONSTRUCTION

The limited-angle projections are reconstructed with the SCoLD method that makes use of the real mask obtained in previous steps. After an optimization process, the regularization parameters selected for the SCoLD reconstruction were:

- α: 0.0003
- μ: 20
- β: 1
- λ: 1
- γ: 0.05
- Number of iterations: 50

The matrix size and voxel size of the reconstruction were the same as for the preliminary FDK reconstruction.

To compare the improvement in image quality by the incorporation of the surface information into the reconstruction process, we compute an approximation of error derived by mask uncertainties.

The test is done using as gold standard the full angle FDK reconstruction comparing it to both iterative reconstructions done using the ideal mask and the real mask. The metric used in this case is the Root-Mean-Square Deviation (RMSD) that estimates the error between two sets of data taking into account every individual pixel values and gives a value.

$$Root\ Mean\ Square\ Deviation\ (RMSD) = \sqrt{\frac{\sum_{i=1}^{n}(X_{1,i} - X_{2,i})}{n}} \quad \text{(Eq. 5.2)}$$

The increment of the error when applying a real mask instead of an ideal one is calculated by the relative error with the following equation:

$$Relative\ Error = \frac{\left|RMSD_{ideal\ iterative} - RMSD_{surface\ iterative}\right|}{RMSD_{ideal\ iterative}} \quad \text{(Eq. 5.3)}$$

where $RMSD_{ideal\ iterative}$ is the RMSD value of iterative reconstruction using ideal mask compared to the FDK standard reconstruction and $RMSD_{surface\ iterative}$ is the RMSD value of iterative reconstruction using real mask compared to the same standard.

6 RESULTS

Fig. 6.1 shows the overlap of the two masks, being the real mask significantly larger than the ideal one. The result of DSC between both masks gives a similarity of 91.34%. The difference is predominantly caused by the hair of the rodent that can be seen by the structured light scanner but it is barely visible in a radiographic image.

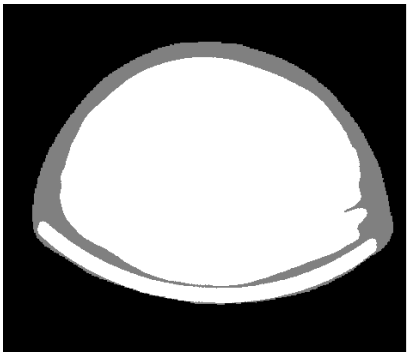

Fig. 6.1: Surface scanner mask (in gray) and ideal mask (in white) overlapped.

Fig. 6.2 shows distortions in shape and streak artifacts in the limited view FDK reconstruction (b), which are compensated using the SCoLD iterative algorithm with the mask constrain (c and d). There are not noticeable differences between the results obtained with the real and the ideal masks.

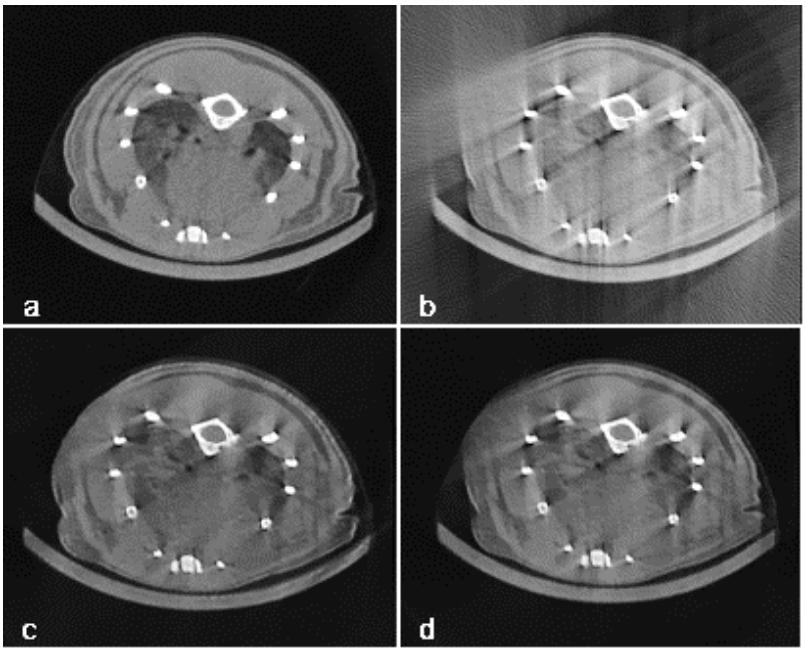

Fig. 6.2: Comparison of reconstructed volumes of a) complete data FDK reconstruction b) FDK reconstruction of limited view of 120º c) iterative reconstruction with ideal mask d) iterative reconstruction using the real mask. Both iterative reconstructions are done using the same parameters.

The RMSD between the gold standard and iterative reconstruction using the ideal mask is 0.8427, while the value is slightly higher, 0.8642, when using the real surface mask. The relative error between both masks gives a 2.55% of difference.

7 DISCUSSIONS AND FUTURE WORK

This work has demonstrated the feasibility to obtain surface information from real data for its use in the reconstruction method SCoLD to improve the image quality in limited-view tomography studies. Since this has been the first attempt to develop a complete workflow for such procedure, there are many aspects that can be optimized for further studies.

To obtain the surface information of the sample, we proposed the use of a light scanner. Among the available 3D scanning technologies described in Section 3, we considered that non-contact structured light scanners are the most suitable for an easy setup in a clinical or preclinical environment. In these scenarios the space is shared by many devices or equipment, so the scanner must be easy to handle, apart from allow a fast scanning process since we are dealing with living organisms and it is required they remain immobile.

We have successfully developed a protocol that extracts the geometrical information from the sample with the scanner *Artec Eva* and make the data useful for iterative reconstruction algorithms. However, the cost of this scanner is relatively higher than others such as *Microsoft Kinect Sensor*, *Cubify Sense* or *XYZprinting*. As a future work, a further analysis of these scanners can be done to examine whether their accuracy is enough for our purpose. Besides it could be also interesting to consider the option of using infrared scanners.

The use of advanced iterative reconstruction methods in scenarios of limited-data allows to reduce the noise and artifacts in the reconstructed images. We have demonstrated that the mask obtained with the scanner from the real data is similar enough to and ideal mask obtained from a CT and therefore can be used as prior information for the reconstruction algorithm. We saw that the main difference between the ideal and the real mask was related to the fur of the animals which is mostly visible with the light scanner but not in CT projections (Fig. 7.1). For future studies, this can be overcame by shaving the animal before the acquisition.

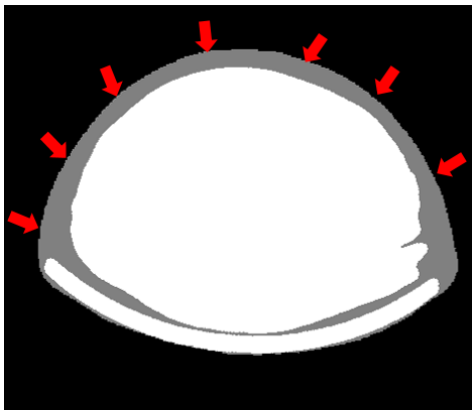

Fig. 7.1: Hair layer of the sample (in gray) present in acquired mask makes it to be larger than the ideal one (in white).

Regarding the markers needed for the registration process, we saw that although they were made of ceramic material, slight artifacts were induced in CT images due to beam hardening effect in nearby areas (Fig. 7.2).

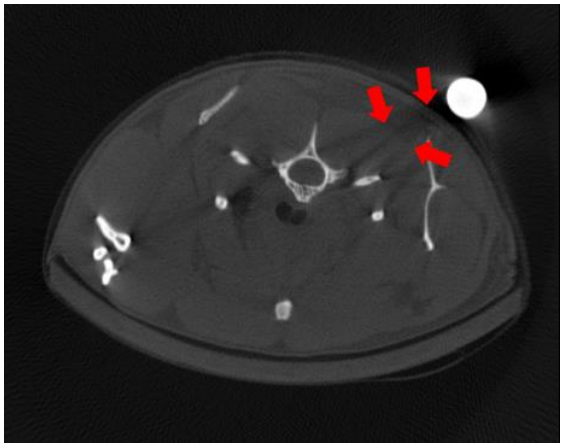

Fig. 7.2: The presence of artifact due to the ceramic marker

As the structured light scanner is able to provide texture information, in future works we can take advantage of this data and greatly reduce the size of the markers, which could be replaced by smaller CT markers with color patterns (Fig.7.3). This will also help to reduce the fiducial registration error since markers can be then placed further apart without exceeding the FOV.

Fig. 7.3: Maker CT-SPOT of 4 mm in diameter used in this work (left) compared to a potential maker of 1.5 mm for texture guided registration.

In this way, after this study, several lines of work are open, as well as the potential to test the proposed workflow in clinical scenarios.

8 PROJECT MANAGEMENT

In this chapter we will present the estimated time inverted in this work and the economic impact it has concerning both the personnel involved and materials used.

8.1 PERSONNEL COST

The total time dedicated to this work is approximately 650 hours by the biomedical engineer while assistance is provided by the research engineer and the supervision is done by the project coordinator. A laboratory technician was needed mainly for the experimental stage.

The gross wage of each is detailed in Table 8.1:

Role	***Dedicated Time (Hours)***	***Wage/hour (€)***	***Cost(€)***
Project Coordinator	150	40	6000
Research Engineer	200	30	6000
Biomedical Engineer	650	20	13000
Total			25000

Table 8.1: Personnel cost breakdown

8.2 MATERIAL COST

Material costs (Table 8.2) derived from this work are mainly concerned on four parts: personal computer (PC) related to auxiliary tasks and processing routines, light scanner and CT acquisition necessities.

Equipment costs are calculated taking into account an amortization of 5 years so that the expenditure is expressed as *Cost/Year*.

Materials	***Unit Cost (€)***	***Cost/Year (€)***	***Dedicated time***	***Cost (€)***
Personal Computer	1000	200	7 months	116.7
GPU	192	38.4	7 months	22.4
Artec Eva	15000	3000	2 months	500
Total				639.1

Table 8.2: Material cost breakdown

8.3 SERVICE COST

Service costs (Table 8.3) are those derived from the acquisition of CT images at Laboratorio de Imagen Médica (LIM) of HGUGM calculated according to the rates provided by Servicio de Apoyo a la Investigación (SAI) of Instituto de Investigación Sanitaria Gregorio Marañón (IiSGM). Details can be found in the link provided:

http://www.iisgm.com/infraestructuras/servicios-de-apoyo-a-la-investigacion/tarifas-sais-vigentes-desde-22042015/

Service	*Cost/Hour (€)*	*Dedicated Time (hours)*	*Cost (€)*
micro PET/CT	65	30	1950
Anesthesia	10	30	300
Laboratory Technician	17	30	510
Total			2760

Table 8.3: Service cost breakdown

8.4 TRAVEL COST

Travel costs are transportation and the accommodation costs derived from attending to the Congreso Anual de la Sociedad Española de Ingeniería Biomédica (CASEIB).

Concept	*Cost (€)*
Transportation	60
Accomodation	112.5
Total	172.5

Table 8.4: Travel expenses

8.5 OTHER EXPENSES

Additional costs were produced by the purchase of the software license of Matlab and the registration fee of CASEIB.

Concept	*Anual fee (€)*
Matlab License	1200
CASEIB registration	200
Total	1400

Table 8.5: Other expenses generated

8.6 INDIRECT COST

Following the legislation of the IiSGM, the indirect cost is calculated as 15% of all costs stated previously. The sum of them gives 29971.6 €. Hence, the indirect cost generated is 4495.7 €.

8.7 TOTAL COST

The total cost of this work is the sum of all previous terms is shown in Table 8.4:

Personnel Cost (€)	25000
Material Cost (€)	639.1
Service Cost (€)	2760
Travel Cost (€)	172.5
Other Expenses (€)	1400
Indirect Cost (€)	4495.7
TOTAL COST (€)	34467.3

Table 8.6: Total Cost

9 APPENDIX

A. SCIENTIFIC PUBLICATIONS DERIVED FROM THIS THESIS

X. Ye, C. de Molina, N. Ballesteros, A. Martínez, M. Desco, M. Abella. Extracción de superficie con escáner de luz estructurada para tomografía de ángulo limitado. Congreso Anual de la Sociedad Española de Ingeniería Biomédica (CASEIB), Bilbao, 2017.

N. Ballesteros, C. de Molina, X. Ye, M. Desco, M. Abella. Surface extraction with structured-light scanner for limited angle tomography. European Molecular Imaging Meeting (EMIM). San Sebastian, 2018. Poster Session

Procesado de Señal Biomédica III — **Miércoles, 29 de Noviembre, 17:30 - 19.00 (Sala Arriaga)**
Moderadores: Luis Coelho y Beatriz Giraldo

Hora	Título	Autores
17:30	Análisis de Fluctuaciones sin Tendencias (DFA) en los Registros de Oximetría para la Ayuda en el Diagnóstico del Síndrome de la Apnea-hipopnea del Sueño Infantil	F. Vaquerizo*, D. Álvarez, L. Kheirandish, G. C. Gutiérrez, V. Barroso-García, R. Romero, A. Crespo, F. del Campo, D. Gozal, R. Hornero
17:45	Towards a Quantification of EEG Brain Activity in the Self-Pacing Regime	J. Silva, A. Martins da Silva, S. Reis*, L. Coelho
18:00	Caracterización de los Patrones de Flujo de Información en el EEG de Pacientes con Deterioro Cognitivo Leve	S. J. Ruiz*, C. Gómez, J. Poza, P. Núñez, V. Rodríguez, M. A. Tola-Arribas, M. Cano, R. Hornero
18:15	Promediado de Potenciales de Acción de Unidad Motora basado en Ventanas Deslizantes	A. Malanda*, I. Rodríguez-Carreño, J. Navallas-Irujo, J. Rodríguez-Falces, M. Fernández-Martínez, L. Gila-Usero
18:30	Improvement of Non-invasive Intrauterine Pressure Estimation based on Electrohysterogram	C. Benalcazar*, C. Sempere, J. Mas, Y. Ye-Lin, J. Alberola, A. Perales, A. López, J. García-Casado, G. Prats
18:45	Caracterización de la Complejidad de la Señal Electrohisterográfica en Mujeres con Amenaza de Parto Prematuro mediante Lempel-Ziv	J. Mas*, Y. Ye-Lin, C. Benalcazar-Parra, J. Alberola-Rubio, A. Perales, J. García-Casado, G. Prats-Boluda

Imagen Biomédica III — **Miércoles, 29 de Noviembre, 17:30 - 19.00 (Sala Oteiza)**
Moderadores: Begoña Acha y Gloria Bueno

Hora	Título	Autores
17:30	Solución Tecnológica para el Cálculo Automático de la Escala de Boston sobre Imágenes Colonoscópicas	Alain Sánchez*
17:45	Detección e Identificación de Vértebras en Imágenes de TC Empleando Técnicas de Inteligencia Artificial y Procesamiento de Imagen	A. Jimenez-Pastor, A. Alberich-Bayarri, B. Fos-Guarinós, F. García-Castro, L. Martí-Bonmatí
18:00	Extracción de Superficie con Escáner de Luz Estructurada para Tomografía de Ángulo Limitado	X. Ye*, C. de Molina, N. Ballesteros, A. Martínez, M. Desco, M. Abella
18:15	Corrección de Artefacto por Movimiento Respiratorio para TAC de Pequeño Animal en Estudios con Bajas Dosis de Radiación	N. Ballesteros*, C. De Molina, M. Desco, M. Abella
18:30	Accurate Lung Segmentation of Thorax CT Images on a Tuberculosis Infection Model	B. Zufiria, L. Fernandez, P. M. Gordaliza, S. Sharpe, M. Desco, A. Munoz-Barrutia*, J. J. Vaquero

Extracción de superficie con escáner de luz estructurada para tomografía de ángulo limitado

X. Ye[1], C. de Molina[1,2], N. Ballesteros[1,2], A. Martínez[2], M. Desco[1,2,3,4], M. Abella[1,2,3,4]

[1] Depto. Bioingeniería e Ingeniería Aeroespacial, Universidad Carlos III de Madrid, España, {monica.abella, manuel.desco}@uc3m.es

[2] Instituto de Investigación Sanitaria Gregorio Marañón, Madrid, España, {desco, mabella}@hggm.es

[3] Centro Nacional de Investigaciones Cardiovasculares Carlos III (CNIC), Madrid, España

[4] Centro de investigación en red en salud mental (CIBERSAM), Madrid, España

Resumen

En una adquisición estándar de TAC se obtiene un número elevado de proyecciones alrededor de la muestra cubriendo un rango angular de 360º. Sin embargo, existen diferentes escenarios en los que únicamente se pueden adquirir pocas proyecciones en un rango angular reducido. La reconstrucción 3D de estos datos limitados requiere métodos avanzados que incorporen información a priori para compensar la falta de datos. En la literatura se ha propuesto el uso de la información de superficie para la recuperación del contorno de la muestra pero únicamente se han evaluado en simulación y su aplicación práctica incluyendo la extracción de la superficie no ha sido explorada.

En este trabajo se propone el uso de un escáner de luz estructurada para la extracción de la superficie y se describe el protocolo completo para la obtención de imagen 3D a partir de datos limitados. El protocolo propuesto se ha evaluado en un estudio de pequeño animal con el escáner de superficie 3D Artec Eva mostrando la viabilidad de la propuesta.

1. Introducción

En una adquisición estándar de TAC se obtiene un número elevado de proyecciones alrededor de la muestra cubriendo un rango angular de 360º. Sin embargo, existen escenarios de tomografía de ángulo limitado en los que se obtiene un número reducido de proyecciones en un rango angular mucho menor de 360º debido a limitaciones de movimientos (durante cirugía, UCI). Así mismo, en aplicaciones como TAC de energía dual o *gating* respiratorio se obtienen conjuntos de proyecciones limitados para cada voltaje de la fuente o para cada fase del ciclo respiratorio respectivamente. La reconstrucción de estos datos de ángulo limitado con métodos convencionales como FDK presenta diferentes artefactos, principalmente rayas y distorsión de los bordes, que afectan gravemente a la calidad de las imágenes finales.

Para reducir estos artefactos, se pueden utilizar métodos avanzados de reconstrucción que compensen la falta de datos incorporando información a priori, resolviéndolo iterativamente como un problema de optimización [1-5]. En [6] los autores propusieron incorporar la superficie de la muestra como información a priori y así ayudar al problema de reconstrucción restringiendo la solución al subespacio comprendido por la superficie. Resultados preliminares demostraron la mejora significativa reduciendo los artefactos y recuperando el contorno de la muestra cuando la información de superficie se añadía al problema. Sin embargo, la evaluación fue solo con simulaciones y su aplicación práctica incluyendo la extracción de la superficie no ha sido explorada.

Para la extracción de esta superficie existen dos tipos de escáneres 3D en función de si hay contacto con el objeto o no. Los primeros aportan suficiente precisión cuando se trata de objetos rígidos. Sin embargo, para el caso de tejido blando se producen deformaciones debido a posibles variaciones en la fuerza de contacto del puntero. Los escáneres 3D sin contacto evitan este problema. Entre ellos, el escáner *ConoProbe Mark*, dispositivo basado en holografía conoscópica [7] que emplea la técnica de interferometría y obtiene puntos en 3D de la superficie integrando las medidas de distancias realizadas con un sistema de posicionamiento basado en cámaras de infrarrojo. Este dispositivo es especialmente útil para cavidades biológicas, superficies reflectantes o transparentes pero supone un tiempo elevado de adquisición. Por otra parte, el escáner de luz *3D Artec Eva* obtiene la superficie en poco tiempo con un dispositivo portátil y no requiere la instalación de cámaras de infrarrojos. Este escáner se basa en la proyección de patrones de luz tipo cuadrícula y en el análisis de la distorsión de dichos patrones. Por estas razones, este escáner es el más adecuado para la obtención de superficie de un paciente en escenarios de radiología.

En este trabajo se presenta un protocolo completo para la obtención de una imagen 3D a partir de datos de tomografía de ángulo limitado. Esto es posible gracias al registro de la superficie de la muestra obtenida con el escáner de luz estructurada *3D Artec Eva* con las proyecciones adquiridas. El proceso completo se ha probado en un TAC de pequeño animal mostrando la viabilidad del protocolo.

2. Generación de superficie

En la Figura 1 se muestra el flujo de trabajo propuesto para la tomografía de ángulo limitado basada en la extracción de superficie con el escáner 3D portátil Artec Eva (Artec3D).

ISBN: 978-84-9082-797-0, pags. 243- 246

Figura 1. *Flujo de trabajo propuesto para tomografía de ángulo limitado*

2.1. Adquisición de datos

Para la adquisición de las proyecciones, se colocan tres marcadores radiopacos no metálicos con un diámetro de 4 mm (Figura 2), suficiente para ser visibles por el escáner 3D y así facilitar el registro de la superficie.

Figura 2. *Posición de los marcadores sobre la muestra bajo estudio*

Se realiza una adquisición TAC de un estudio de roedor utilizando el escáner de pequeño animal Argus PET/TAC (Sedecal) [8] con los siguientes parámetros: 340 µA, 45 KeV y 360 proyecciones con tamaño de píxel de 0.2 mm. Para simular la obtención de datos de ángulo limitado se seleccionan solo 45 proyecciones en un rango angular limitado de 90º.

A continuación, adquirimos la superficie con el escáner 3D *Artec Eva* realizando un barrido alrededor de la muestra cubriendo todos los ángulos como se aprecia en la Figura 3.

Figura 3. *Captura de la superficie de la muestra con el escáner 3D Artec Eva*

2.2. Generación de máscara de superficie

Utilizamos el propio software del escáner, *Artec Studio*, para generar el archivo *.stl* que contiene la malla poligonal a partir de la cual se generará la máscara.

Para ello, fusionamos diferentes barridos con la opción *fusion* generando el resultado mostrado en la Figura 4-A.

A continuación, se limpian todos los objetos que no pertenecen a la muestra con la herramienta manual *Eraser* generando la imagen mostrada en Figura 4-B.

Para el resto de objetos pequeños y desconectados que no han sido eliminados manualmente se utiliza un filtro (opción *Small Objects Filter*) que nos permite quedarnos únicamente con la muestra.

Tras este paso, es importante cubrir todos los agujeros, huecos y bordes con *Hole filling* para generar un volumen cerrado (Figura 4-C).

Finalmente, se centra la malla generada en el sistema de coordenadas deseado (Figura 4-D).

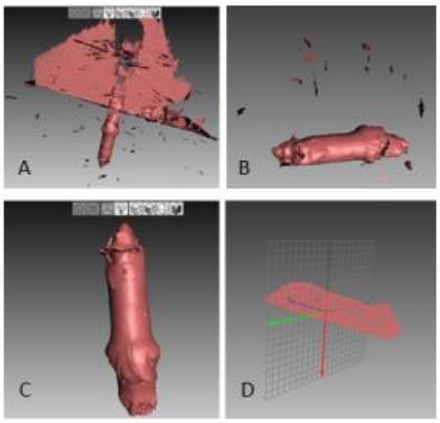

Figura 4. *A: datos crudos fusionados sin procesar; B: datos limpiados de objetos grandes; C: datos limpios de objetos pequeños y con las cavidades rellenas; D: datos centrados*

El resultado es una malla con la información de los vértices y caras de los polígonos que la forman. Para generar la máscara es necesario convertir los vértices en coordenadas de vóxel asignando "1" a los vóxeles delimitados por la malla y "0" a los vóxeles del fondo. Esto se realiza con la función *Polygon2Voxel* de Dirk-Jan Kroon [9] en Matlab que subdivide los polígonos hasta que el borde más largo mida menos de la mitad de la dimensión del vóxel.

2.3. Registro

La máscara generada anteriormente contiene el volumen entero de la muestra y es necesario corresponder la máscara con la región adquirida en el TAC.

Para ello, se realiza una reconstrucción previa usando *Mangoose* [10], método basado en FDK sobre la que se segmentan los marcadores de forma manual. La correspondencia entre esta reconstrucción previa y la máscara generada se realiza mediante un registro rígido por marcadores con la herramienta *3D Slicer* (https://www.slicer.org/). Como resultado obtenemos la máscara orientada y ajustada al campo de visión

adquirido en el TAC. Finalmente con este resultado se realiza un registro más fino basado en información mutua.

La Figura 5 muestra la correspondencia entre la máscara obtenida con el escáner 3D sobre la imagen obtenida a partir de la reconstrucción de datos completos (referencia).

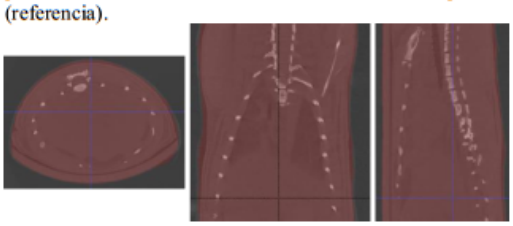

Figura 5. *Máscara obtenida con el escáner de superficie (en rojo) superpuesta con la imagen TAC de datos completos (referencia)*

Para la evaluación del método se obtiene la máscara ideal a partir de la segmentación de la imagen TAC referencia mediante umbralización y posterior procesamiento morfológico. La Figura 6 muestra la máscara ideal (en blanco) sobre la máscara obtenida con el escáner de superficie. Para su evaluación cuantitativa se ha calculado el índice Sørensen-Dice entre la máscara escaneada y la ideal que nos indica que existe un 94.92% de similitud entre ambas máscaras.

Figura 6. *Rodaja central de la máscara obtenida con el escáner de superficie (en gris) superpuesta con la misma rodaja de la máscara ideal (en blanco)*

3. Reconstrucción avanzada

Las proyecciones de ángulo limitado se reconstruyen con el método iterativo avanzado propuesto en [6] que hace uso de la máscara de superficie obtenida en los pasos previos. Los parámetros de regularización, que se han obtenido empíricamente, son μ=20, α=0.003, λ=1, β=1, γ=0.1 y un número de iteraciones de 35.

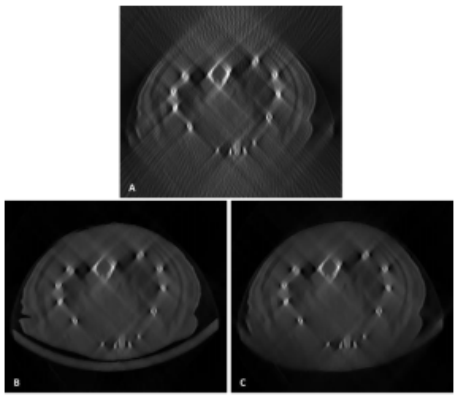

Figura 7. *Reconstrucción de la rodaja central con el método convencional FDK (A) y con el método de reconstrucción iterativo usando la máscara ideal (B) y la máscara obtenida con el escáner de superficie propuesto (C)*

En el panel A de la Figura 7 se muestra la rodaja central de la reconstrucción previa (FDK), donde se pueden apreciar las bandas y la distorsión del contorno de la muestra debido a la falta de proyecciones y al rango angular limitado. Los paneles B y C muestran el resultado obtenido con el método iterativo avanzado. En ambos casos se recupera correctamente el contorno de la muestra además de reducir los artefactos de bandas. El resultado es similar cuando la máscara ha sido obtenida con el escáner de superficie (Figura 7-C) a la obtenida con la máscara ideal (Figura 7-B).

4. Conclusiones y discusión

Se ha presentado un protocolo completo para la obtención de imagen 3D en escenarios de tomografía con datos limitados.

La falta de datos se compensa con un algoritmo de reconstrucción avanzado que incorpora información de la superficie del paciente. Los resultados obtenidos muestran la viabilidad del uso de un escáner de luz para la extracción de la superficie cuando se adquieren pocas proyecciones en un rango angular muy reducido.

La máscara obtenida con el protocolo propuesto presenta una gran similitud (94.92%) con la máscara ideal obtenida a partir de la imagen TAC. El protocolo propuesto hace uso de un escáner de luz que permite escanear la muestra fácilmente en poco tiempo, sin necesidad de instalación de cámaras de infrarrojos y evitando los problemas adheridos a los sistemas de superficie que requieren contacto directo con la muestra.

La mayor limitación de este trabajo se encuentra en el registro entre la máscara y la reconstrucción previa. Debido a que esta reconstrucción se hace a partir de datos limitados con un método de reconstrucción convencional, presenta muchos artefactos dificultando la segmentación de los marcadores. Además, se utilizan marcadores de uso clínico con un tamaño elevado para estudios de pequeño animal.

Como trabajo futuro se propone hacer uso de la información de textura proporcionada por el escáner de superficie para la mejora del proceso de registro.

5. Agradecimientos

Este trabajo ha sido financiado por el Ministerio de Economía, Industria y Competitividad (proyectos DPI2016-79075-R) y el Instituto de Salud Carlos III (proyecto DTS17/00122).

Referencias

[1] Matenine D, G.Y., Després P, *GPU-accelerated regularized iterative reconstruction for few-view cone beam CT*. Medical Physics, 2015. **42**(4): p. 1505-17.

[2] Duan, X., et al., *Few-View Projection Reconstruction With an Iterative R*econstruction-Reprojection Algorithm and TV Constraint. IEEE Transactions on Nuclear Science, 2009. **56**(3): p. 1377-1382.

[3] LaRoque, S.J., E.Y. Sidky, and X. Pan, *Accurate image reconstruction from few-view and limited-angle data in diffraction tomography*. Journal of the Optical Society of America. A, Optics, image science, and vision, 2008. **25**(7): p. 1772-1782.

[4] Molina, C.d., et al. *Evaluation of the possibilities of limited angle reconstruction for the use of digital Radiography system as a tomograph*. in 2014 IEEE Nuclear Science Symposium and Medical Imaging Conference (NSS/MIC). 2014.

[5] J. Velikina, S.L., G-H. Chen, *Limited view angle tomographic image reconstruction via total variation minimization*. Proc. SPIE 6510, Medical Imaging 2007: Physics of Medical Imaging, 2007.

[6] Molina C de, Abascal JFPJ, Desco M, Abella M. *Study of the possibilities of Surface-Constrained Compressed Sensing (SCCS) Method for Limited-View Tomography in CBCT systems*. Proceedings of 4th International Conference on Image Formation in X-Ray Computed Tomography, 2016

[7] Alvarez I, Enguita JM, Frade M, Marina J, Ojea G. *On-line metrology with conoscopic holography: beyond triangulation*. Sensors (Basel), 9(9), 7021-37, 2009

[8] Vaquero, J. J., Redondo, S., Lage, E., Abella, M., Sisniega, A., Tapias, G., Desco, M. ., *"Assessment of a new high-performance small-animal x-ray tomograph*, IEEE Transactions on Nuclear Science, vol. 55, pp. 898-905, 2008.

[9] D.Kroon, University of Twente (May 2009). https://es.mathworks.com/matlabcentral/fileexchange/24086-polygon2voxel?s_tid=prof_contriblnk

[10] Abella, M., J.J. Vaquero, A. Sisniega, J. Pascau, A. Udías, V. García, I. Vidal, and M. Desco, Software Architecture for Multi-Bed FDK-based Reconstruction in Xray CT Scanners. Computer methods and programs in biomedicine, 2011. (in press). 685618.

X-Ray Imaging Technology

Session chair: **Claudia Kuntner** - Vienna, Austria; **Christian Dullin** - Göttingen, Germany

Shortcut: **PW-08**
Date: **Thursday, 22 March, 2018, 11:30 AM**
Room: **Banquet Hall | level -1**
Session type: **Poster Session**

Abstract

Click on an contribution preview the abstract content.

082 **Spectral photon-counting CT of lungs of mice infected with Mycobacterium Tuberculosis: potential for locating Tuberculosis involvement** (#82)

A. Ortega-Gil[1, 2], M. Moghiseh[3], C. Lowe[3], A. Muñoz-Barrutia[1, 2], A. Raja[3], A. P. H. Butler[3, 4, 5], J. J. Vaquero[1, 2], N. G. Anderson[3]

083 **A complete quantification study on x-ray image contrast induced by gold nanoparticles for planar imaging and Computed Tomography at preclinical and clinical energies** (#258)

M. Rouchota[1, 2], S. Neyt[3], R. Van Holen[3], G. Kagadis[1], G. Loudos[2, 4, 5]

084 **Combined mouse brain and whole body skeleton imaging within a single µCT scan** (#372)

S. Llambrich Ferré[1], J. Wouters[1], N. Martínez-Abadías[2, 3, 4], G. Vande Velde[1]

085 **High resolution visualization and quantification of murine renal fibrosis by micro computed tomography** (#341)

J. Missbach-Guentner[1], D. Pinkert-Leetsch[1], C. Dullin[1, 2], D. Hornung[3], B. Tampe[4], M. Zeisberg[4], F. Alves[1, 5, 6]

086 **Tumour Volume Measurement. Reliability and Accuracy of Calliper vs uCT in a Xenograph Breast Cancer Murine Model** (#44)

J. A. Camara[1], A. Pujol[1], A. Martín-Pardillos[2, 3], S. Ramon y Cajal[2, 3]

087 **Longitudinal Imaging of an Intravenous Lung Tumour Murine Model. Comparison of Optical Imaging and uCT Techniques** (#48)

J. A. Camara[1], A. Pujol[1]

088 **µCT imaging approach for mouse lung fibrosis detection induced by bleomycin osmotic mini pump** (#558)

F. Ruscitti[1], S. Belenkov[2], F. Ravanetti[3], V. Bertani[3], R. Ciccimarra[3], V. Menozzi[3], J. Essers[4], Y. Ridwan[4], A. KleinJan[5], P. Van Heijningen[4], A. Cacchioli[3], M. Civelli[1], G. Villetti[1], F. F. Stellari[1]

089 **Calibration set-up for Dual Energy capabilities in a Real Advance Digital Radiography System** (#349)

C. de Molina[1, 2], C. Martínez[1, 2], M. Desco Menéndez[1, 2, 3], M. Abella Garcia[1, 2, 3]

090 **Recovering density values on small animal X-ray imaging through beam hardening compensation: preliminary results** (#280)

C. Martínez[1, 2], N. Ballesteros[1, 2], C. de Molina[1, 2], M. Desco Menéndez[1, 2, 3], M. Abella Garcia[1, 2, 3]

091 **X-Ray scatter correction in 2D radiography using a beam-stopper: a simulation study** (#272)

A. Martinez Martinez[1], C. Martinez Sanchez[2], M. Desco Menéndez[1, 2, 3], M. Abella Garcia[2, 3]

092 **Surface extraction with structured-light scanner for limited angle tomography** (#291)

N. Ballesteros[1, 2], C. de Molina[1, 2], X. Ye[1], M. Desco Menéndez[1, 2, 3], M. Abella Garcia[1, 2, 3]

Surface extraction with structured-light scanner for limited-angle tomography

N. Ballesteros[2], C. de Molina[1,2], X. Ye[1], M. Desco[1,2,3,4], M. Abella[1,2,4]

[1] *Departamento de Bioingeniería e Ingeniería Aeroespacial, Universidad Carlos III, Madrid, Spain*
[2] *Instituto de Investigación Sanitaria Gregorio Marañón (IISGM), Madrid, Spain*
[3] *Centro de Investigación en Red de Salud Mental (CIBERSAM, CIBER CB07/09/0031), 28007 Madrid, Spain*
[4] *Centro Nacional de Investigaciones Cardiovasculares Carlos III (CNIC), Madrid, Spain.*

INTRODUCTION

- Some clinical scenarios are not indicated for CT and only few projections can be obtained within a reduced angular range
- The use of conventional methods, like FBP, to reconstruct these limited data results in artifacts (streaks and shape distortion) in the final images

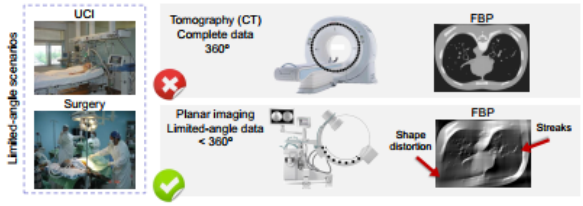

- Advanced reconstruction methods can compensate the lack of projections by including prior information
- The surface of the sample has been shown to be a good prior in this context with the SCoLD reconstruction method (*Molina, C. de, et al. Proceedings of 4th CT Meeting, 2016)*

- We propose a protocol to extract the surface of the sample in real limited-angle scenarios using a structured-light 3D scanner

METHODS

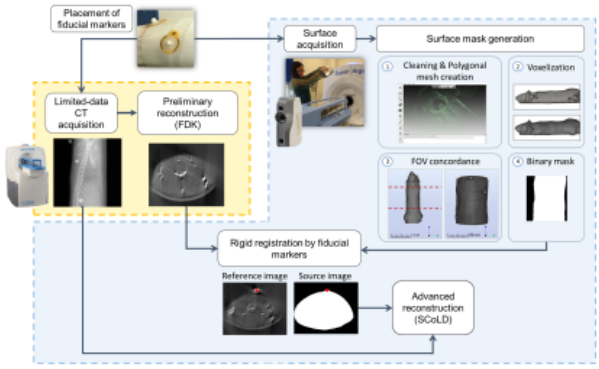

Evaluation

- Rodent data was acquired in the SuperArgus PET/CT (Sedecal), 340 μA, 45 KeV
  - Three 4mm Ø non-metallic radiopaque markers
  - Limited data: 45 projections over 120º
  - Complete data: 360 projections over 360º
- Regularization parameters for SCoLD algorithm: μ=20, α=0.003, λ=1, β=1, γ=0.1, with 35 iterations
- An ideal mask is obtained by thresholding of the complete data

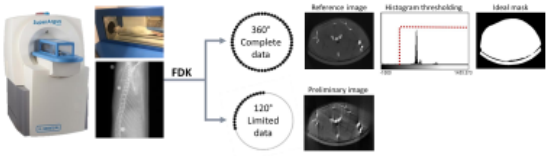

- Surface error: Sørensen-Dice index (SD)

$$SD = \frac{2\times|Maskideal \cap Maskscanner|}{|Maskideal|+|Maskscanner|}$$

- Effect on the reconstruction: Root Mean Square Error (RMSE)

$$RMSE = \sqrt{\frac{\sum_{m=0}^{M-1}\sum_{n=0}^{N-1}(CT(m,n) - SCoLD(m,n))^2}{MN}}$$

RESULTS

- Quality of the mask acquired
  - The Sørensen-Dice index showed a 94.92% of similarity between the acquired mask with the surface scanner and the ideal one
  - The main difference between the ideal mask (white) and the acquired mask (gray) is due to the hair of the animal, seen by the light scanner but invisible for the CT system

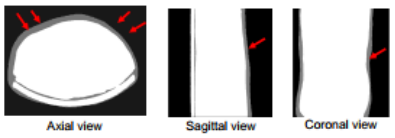

- Effects on the reconstructed image
  - Preliminary reconstruction image shows streaks and edge distortion as a consequence of the limited angular range
  - Using the surface information of the sample the contour of the sample is properly recovered and the streaks artifacts are diminished
  - The effect of using the mask obtained from the surface scanner increases the error only in 2.44%

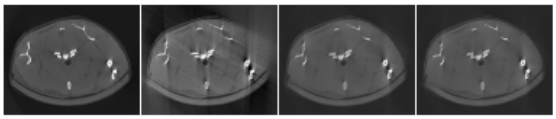

Reference image (FDK with complete data)	Preliminary image (FDK with limited data)	SCoLD + ideal mask from reference image RMSE=2,252	SCoLD + Surface scanner mask RMSE=2,307

CONCLUSIONS

- We present a complete protocol to obtain tomographic images in scenarios of limited-angle data using an advanced reconstruction algorithm that exploits the surface information of the sample
- Results on rodent studies showed the viability of a structured-light scanner for the extraction of the surface
- This technology allows short scan times, avoiding the need for any additional hardware installation or contact with the sample

Acknowledgements. This work was partially supported by the Ministry of Economy, Industry and Competitiveness (DPI2016-79075-R) and ISCIII-FIS grants DTS17/00122, co-financed by ERDF (FEDER) Funds from the European Commission, "A way of making Europe". The CNIC is supported by the Ministry of Economy, Industry and Competitiveness (MEIC) and the Pro CNIC Foundation, and is a Severo Ochoa Center of Excellence (SEV-2015-0505).

10 GLOSSARY

ARCOS	Computer Architecture and Technology Area
BiiG	Biomedical Imaging and Instrumentation Group
BP	Backprojection
CASEIB	Congreso Anual de la Sociedad Española de Ingeniería Biomédica
CCD	Charge-Coupled Device
CMM	Coordinate Measuring Machine
CT	Computed Tomography
DR	Digital Radiography
DSC	Dice Similarity Coefficient
EM	Electromagnetic
FBP	Filtered Back Projection
FDK	Feldkamp, Davis and Kress cone beam FBP reconstruction
FOV	Field Of View
FPD	Flat Panel Detectors
fps	frames per second
GPU	Graphic Processing Unit
HGUGM	Hospital General Universitario Gregorio Marañón
ICU	Intensive Care Unit
IiSGM	Instituto de Investigación Sanitaria Gregorio Marañón
LIM	Laboratorio de Imagen Médica
ODD	Object-Detector Distance
PC	Personal Computer
RMSD	Root Mean Square Deviation
SAI	Servicio de Apoyo a la Investigación
SCoLD	Surface Constrained method for Limited-Data Tomography
SDD	Source-Detector Distance
SEDECAL	Sociedad Española de Electromedicina y Calidad
SNR	Signal to Noise Ratio
SOD	Source-Object Distance
TV	Total Variation
UMCE	Unidad de Medicina y Cirugía Experimental
UV	Ultraviolet

11 BIBLIOGRAPHY

[1] J. Daniels, "The x rays," *Science,* vol. 3, pp. 562-563, 1896.

[2] J. Beutel, H. L. Kundel, and R. L. Van Metter, *Handbook of Medical Imaging: Physics and psychophysics*, Ilustrated ed. vol. 1: SPIE Press, 2000.

[3] D. Oborska-Kumaszyńska and S. Wiśniewska-Kubka, "Analog and digital systems of imaging in roentgenodiagnostics," *Polish journal of radiology,* vol. 75, p. 73, 2010.

[4] W. A. Kalender, *Computed tomography: fundamentals, system technology, image quality, applications*: John Wiley & Sons, 2011.

[5] R. C. Orth, M. J. Wallace, M. D. Kuo, and T. A. C. o. t. S. o. I. Radiology, "C-arm cone-beam CT: general principles and technical considerations for use in interventional radiology," *Journal of Vascular and Interventional Radiology,* vol. 19, pp. 814-820, 2008.

[6] C. Floridi, A. Radaelli, N. Abi-Jaoudeh, M. Grass, M. De Lin, M. Chiaradia*, et al.*, "C-arm cone-beam computed tomography in interventional oncology: technical aspects and clinical applications," *La radiologia medica,* vol. 119, pp. 521-532, 2014.

[7] M. B. G. d. Silva and E. F. Sant'Anna, "The evolution of cephalometric diagnosis in Orthodontics," *Dental press journal of orthodontics,* vol. 18, pp. 63-71, 2013.

[8] M. Abella, "Contributions to Image Reconstruction in High-Resolution Multimodality Systems for Preclinical Applicaions," Unidad de Medicina y Cirugía Experimental. Hospital General Universitario Gregorio Marañón, Universidad Politécnica de Madrid, Madrid, 2010.

[9] L. Feldkamp, L. Davis, and J. Kress, "Practical cone-beam algorithm," *JOSA A,* vol. 1, pp. 612-619, 1984.

[10] L. L. Geyer, U. J. Schoepf, F. G. Meinel, J. W. Nance Jr, G. Bastarrika, J. A. Leipsic*, et al.*, "State of the art: iterative CT reconstruction techniques," *Radiology,* vol. 276, pp. 339-357, 2015.

[11] R. Rangayyan, A. P. Dhawan, and R. Gordon, "Algorithms for limited-view computed tomography: an annotated bibliography and a challenge," *Applied optics,* vol. 24, pp. 4000-4012, 1985.

[12] R. A. Kleinerman, "Cancer risks following diagnostic and therapeutic radiation exposure in children," *Pediatric radiology,* vol. 36, pp. 121-125, 2006.

[13] E. Ron, B. Modan, J. D. Boice Jr, E. Alfandary, M. Stovall, A. Chetrit*, et al.*, "Tumors of the brain and nervous system after radiotherapy in childhood," *New England Journal of Medicine,* vol. 319, pp. 1033-1039, 1988.

[14] S. Abbas, T. Lee, S. Shin, R. Lee, and S. Cho, "Effects of sparse sampling schemes on image quality in low- dose CT," *Medical physics,* vol. 40, 2013.

[15] C. H. McCollough, L. Yu, J. M. Kofler, S. Leng, Y. Zhang, Z. Li*, et al.*, "Degradation of CT low-contrast spatial resolution due to the use of iterative reconstruction and reduced dose levels," *Radiology,* vol. 276, pp. 499-506, 2015.

[16] S. T. Schindera, D. Odedra, S. A. Raza, T. K. Kim, H.-J. Jang, Z. Szucs-Farkas*, et al.*, "Iterative reconstruction algorithm for CT: can radiation dose be decreased while low-contrast detectability is preserved?," *Radiology,* vol. 269, pp. 511-518, 2013.

[17] C. de Molina, J. F. P.-J. Abascal, J. Pascau, M. Desco, and M. Abella, "Evaluation of the possibilities of limited angle reconstruction for the use of digital Radiography system as a tomograph," in *Nuclear Science Symposium and Medical Imaging Conference (NSS/MIC), 2014 IEEE*, 2014, pp. 1-4.

[18] X. Duan, L. Zhang, Y. Xing, Z. Chen, and J. Cheng, "Few-view projection reconstruction with an iterative reconstruction-reprojection algorithm and TV constraint," *IEEE Transactions on Nuclear Science,* vol. 56, pp. 1377-1382, 2009.

[19] C. de Molina, J. Abascal, M. Desco, and M. Abella, "Study of the possibilities of surface-constrained compressed sensing (SCCS) method for limited-view tomography in CBCT systems," in *Proceedings of the 4th International Meeting on Image Formation in X-Ray CT*, 2016, pp. 491-494.

[20] G. Sansoni, M. Trebeschi, and F. Docchio, "State-of-the-art and applications of 3D imaging sensors in industry, cultural heritage, medicine, and criminal investigation," *Sensors,* vol. 9, pp. 568-601, 2009.

[21] M. Brudfors, V. García- Vázquez, B. Sesé- Lucio, E. Marinetto, M. Desco, and J. Pascau, "ConoSurf: Open- source 3D scanning system based on a conoscopic holography device for acquiring surgical surfaces," *The International Journal of Medical Robotics and Computer Assisted Surgery,* vol. 13, 2017.

[22] U. Ozsoy, R. Sekerci, and E. Ogut, "Effect of sitting, standing, and supine body positions on facial soft tissue: Detailed 3D analysis," *International journal of oral and maxillofacial surgery,* vol. 44, pp. 1309-1316, 2015.

[23] M. Abella, J. J. Vaquero, A. Sisniega, J. Pascau, A. Udías, V. García*, et al.*, "Software architecture for multi-bed FDK-based reconstruction in X-ray CT scanners," *Computer methods and programs in biomedicine,* vol. 107, pp. 218-232, 2012.

[24] J. G. Blas, M. Abella, F. Isaila, J. Carretero, and M. Desco, "Surfing the optimization space of a multiple-GPU parallel implementation of a X-ray tomography reconstruction algorithm," *Journal of Systems and Software,* vol. 95, pp. 166-175, 2014.

[25] D.-J. Kroon, "polygon2voxel," ed. University of Twente, 2009, p. A matlab function that converts a triangulated mesh into a voxel volume

[26] M. Abella, E. Serrano, J. Garcia-Blas, I. García, C. De Molina, J. Carretero*, et al.*, "FUX-Sim: Implementation of a fast universal simulation/reconstruction framework for X-ray systems," *PloS one,* vol. 12, p. e0180363, 2017.

[27] T. Goldstein and S. Osher, "The split Bregman method for L1-regularized problems," *SIAM journal on imaging sciences,* vol. 2, pp. 323-343, 2009.

[28] R. Cheung, "nSPIRE utility to calculate DICE Coefficient," ed: MathWorks, 2012, p. his programs calculate and visualize the dice similarity (volume overlap) of 2D binary images.